Master's thesis

NTNU
Norwegian University of Science and Technology
Faculty of Natural Sciences
Department of Physics

Jørgen Salvesen

Design, test and implementation of a UV 355 nm LIDAR depolarization channel to characterize particles in the atmosphere above ALOMAR

Master's thesis in MLREAL
Supervisor: Patrick Joseph Espy
June 2023

NTNU
Norwegian University of
Science and Technology

Jørgen Salvesen

Design, test and implementation of a UV 355 nm LIDAR depolarization channel to characterize particles in the atmosphere above ALOMAR

Master's thesis in MLREAL
Supervisor: Patrick Joseph Espy
June 2023

Norwegian University of Science and Technology
Faculty of Natural Sciences
Department of Physics

NTNU
Norwegian University of
Science and Technology

Abstract

Aerosols have long been known to provide a net cooling effect on Earth's climate, although the individual contribution of some aerosols to radiative forcing is still unknown. Understanding these atmospheric particles may offer part of the solution to rapid climate change. To investigate particles in the atmosphere above ALOMAR, a 355 nm lidar depolarization channel was designed and tested. However, due to issues with the troposphere laser, the channel has yet to be implemented. Theoretical background and analysis of previous results are also included.

Sammendrag

Det har lenge vært kjent at aerosoler gir en netto avkjølede effekt i klimabalansen, likevel er det individuelle strålingspådrivet til noen aerosoler fremdeles ukjent. En større forståelse for disse atmosfæriske partiklene kan potensielt resultere i en del av løsningen på global oppvarming. For å utforske partikler i atmosfæren over ALOMAR har en 355 nm lidar depolariserings kanal blitt designet og testet. Grunnet problemer med troposfære laseren har kanalen ikke blitt installert. Teoretisk bakgrunn og analyse av tidligere resultater er inkludert i oppgaven.

Acknowledgements

I would like to express my gratitude to my supervisor, Professor Patrick Joseph Espy, for sharing his extensive insights in atmospheric physics and providing an endless stream of potential solutions. I also wish to thank my supervisors at Andøya Space, Dr. Michael Gausa and Martin Flügge, for funding and enabling this thesis.

Contents

Figures

Tables

Chapter 1

Introduction

1.1 Relation to the Specialization Project

During the fall of 2022, I completed a specialization project titled "Design of a UV 355 nm LIDAR depolarization channel to characterize particles in the atmosphere above ALOMAR" [1]. The specialization project provided me with the necessary theoretical background to understand and implement the system.

Work from the specialization project has been incorporated into the master's thesis. Some of the material has been modified or improved, but it is based on the specialization project. The specialization project will not be referenced further in the text; instead, the original sources will be cited. The chapters containing reused material are listed below:

- Introduction 1.2 - 1.3
- Background theory 2.1 - 2.7
- Optical setup 3.1 - 3.7
- Data processing 4.2 - 4.7

1.2 Background and motivation

In recent years there has been a shift in political focus towards global warming caused by rapid climate change. The emission of greenhouse gasses, consisting of primarily carbon dioxide (CO_2) and methane (CH_4), is the leading cause of rapid climate change. Human activities are responsible for almost all atmospheric increase in greenhouse gasses, with the burning of fossil fuels being the main source of emissions [2]. Due to this, political agreements have been implemented in order to decrease emission of greenhouse gasses and limit further global warming. During the twenty-first session of the Conference of the Parties (COP 21) in December 2015, 196 parties signed The Paris Agreement, a legally binding international treaty on climate change. The goal of the agreement is to limit global warming to below two degrees Celsius [3]. To reach this goal measurements of

the atmospheric composition is necessary. Both for measurements of change, but also for understanding of atmospheric composition. Aerosols, a collective term for tiny liquid or solid particles in stable suspension in the atmosphere, contribute to Earth's climate with a net cooling effect through direct aerosol interaction as well as cloud albedo effects [4].

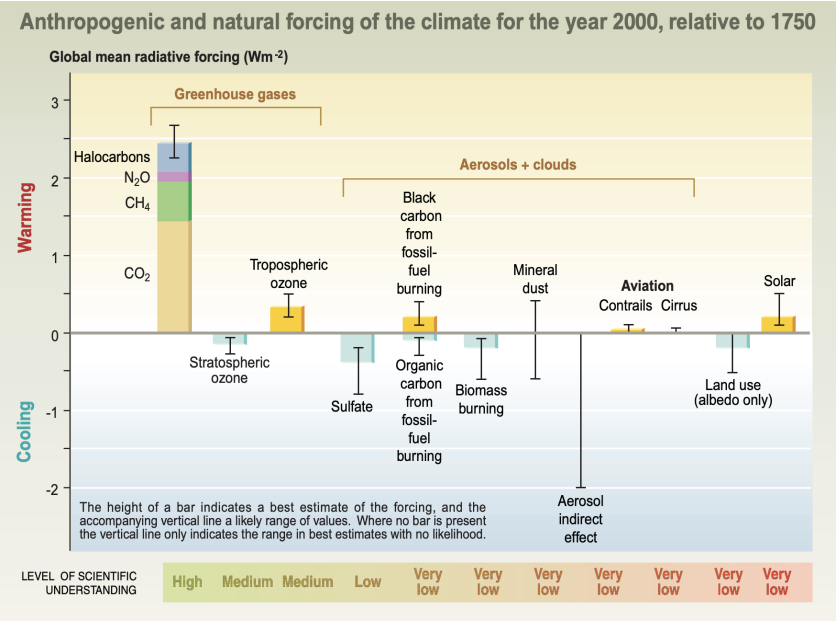

Figure 1.1: The influence of external factors on climate compared using radiative forcing, with their respective levels of scientific understanding [5].

In 2001 the Intergovernmental Panel on Climate Change (IPCC) published a synthesis report on climate change. In this report a figure of anthropogenic and natural forcing was included, as well as the relative level of scientific understanding related to the anthropogenic and natural contributors. The discussed figure is included as figure 1.1, where the bars represent estimates connected to contributions to these radiative forcings, while the vertical lines about the bars represents a range of estimates based on published values and physical understanding of the forcings. With this report IPCC underlines that the understanding of aerosols impact on global climate is quite lacking. Furthermore, aerosol cooling events due to volcanic eruption and aerosols' indirect effect on cloud lifetime is not included. The major uncertainties and missing aerosol effects can further change aerosols potential cooling effect, if properly understood. While long-term measurements of aerosols (e.g. by Putaud *et al.* [6]) and remote sensing (e.g. by Holben *et al.* [7]) have increased knowledge about the composition and characteristics of atmospheric aerosols, an understanding of the greater complexity as well as some aerosols individual contribution to radiative forcing is still unknown [4]. Some research indicate that a better understanding of aerosols and their effects on cli-

mate could provide a potential part of the solution to rapid climate change, by for instance an increase in anthropogenic aerosols emitted to the atmosphere [8].

Furthermore the EarthCARE (Cloud Aerosol and Radiation Explorer) satellite, excpected to launch in 2024, will travel above ALOMAR (Arctic Lidar Observatory for Middle Atmosphere Research) using a atmospheric lidar to provide vertical profiles of aerosols and thin clouds. This is achived by operating at a wavelength of 355 nanometers (nm) with a high spectral resolution receiver and depolarisation channel. Thus a stationary 355 nm depolarization channel at ALOMAR to complement and provide context for the satellite measurements with ground measurements is advantageous and could further advance our understanding of cloud and aerosol effect on climate.

1.3 Scope

The purpose of this master project is to present the design, tests and implementation of a ultraviolet (UV) 355 nm depolarization channel at ALOMAR. A further theoretical background, data processing involved with a depolarized signal, experimental and final results as well as modifications from design to implementation will also be presented.

ALOMAR is an observatory located at 69°N and 16°E, 379 m above the ocean and is operated by Andøya Space. As ALOMAR is placed quite remotely, but close to the Gulf stream, a high variety of both natural and anthropogenic atmospheric particles is to be expected from land, sea and the arctic climate. The high latitude placement also present ALOMAR as a reference station for almost unpolluted, clean air from north and north-western airmasses [9]. The implementation of a 355 nm depolarization channel has several useful applications; for example, complementing measurements of the EarthCARE satellite as well as providing vertical profiles of aerosols and thin clouds that affect the radiative balance in the artic climate. At ALOMAR a 532 nm depolarization channel is already in place. By utilizing results from the 532 nm channel in combination with the 355 nm channel one can extend the particle size range and achieve more accurate results for atmospheric and cloud composition. The expected backscatter returns from ice crystals in cirrus clouds is for instance exemplified in a paper by Kustova *et al.* [10, 11], while aerosol returns have been presented by for instance Giannakaki *et al.* [12] and Müller *et al.* [13]. Using the wavelength pair 532 nm and 355 nm in combination with the beam polarization one can further investigate the Ångström exponent as both a particle size indicator, but also a particle shape indicator in a atmospheric particle mixture [14].

Lidars are often used for temperature profiling of the troposphere, this is also possible with the UV channel [15]. Lidars can have other applications as well, measurement of; height, cloud layers and density, pressure, global wind and trace gas

concentration [16]. These will not be subject to investigation during this masters project.

Chapter 2

Background theory

Lidar, an acronym for Light detection and ranging, is an optical remote sensing device capable of detecting backscattered light from distant particles. A typical lidar setup is shown in figure 2.1. As seen, this setup consists of a transmitter and a receiver. Short light pulses in the order of nanoseconds (ns) are generated from the laser. A beam expander is applied within the transmitter to reduce the divergence of the laser pulses before being transmitted to the atmosphere. Due to interaction with either aerosols or molecules the laser pulses will scatter. As part of the receiver a telescope collects the scattering of light in a backwards direction (i.e. backscattering). The telescope is followed by an optical analyzing system which selects specific wavelengths and polarization states from the collected light. Using photomultiplier tubes, PMTs, the backscattered signal, is converted to an electrical signal. The current produced from the PMTs can be measured directly allowing access to information about properties of the scattering medium.

2.1 Ultraviolet light

UV light is a region of electromagnetic wavelengths shorter than visible light. UV light spans from 380 to 100 nanometers (nm), sometimes subdivided into UV-A, UV-B and UV-C, with ranges 380-315 nm, 315-280 nm, 280-100 nm respectively. Due to absorbtion in the ozone layer of earth's atmosphere, roughly 99% of UV radiation that reaches the earth's surface is in the UV-A band [17]. Hence, the application of a UV depolarization channel in the UV-A range. Executing the implementation of the proposed UV 355 nm depolarization channel will open several possibilities for further investigation. While visible 532 nm channel is most commonly used for lidar signals, the shorter UV 355 nm wavelength channel offers eye saftey and stronger Rayleigh scattering [15].

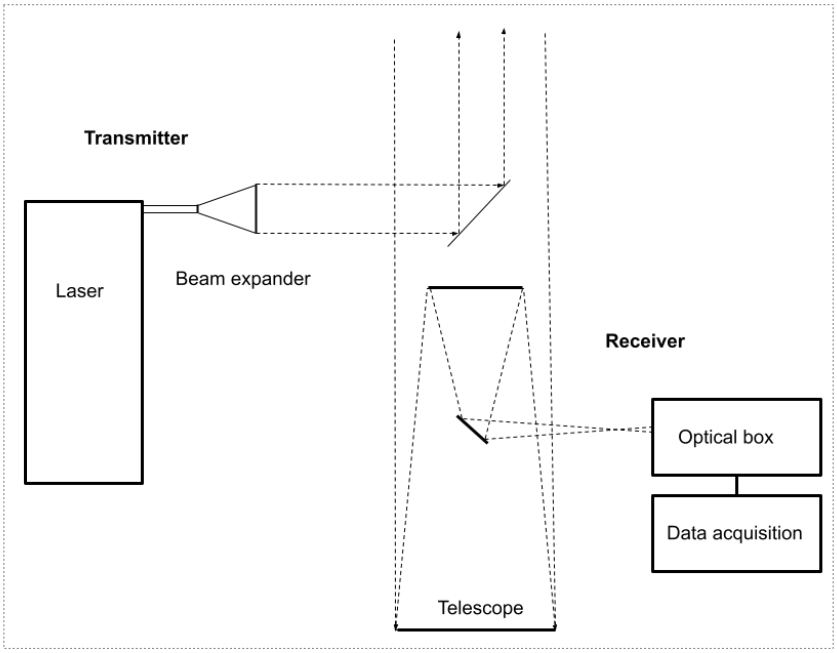

Figure 2.1: A typical lidar setup.

2.2 Polarization and depolarization

If a laser beam consist of only electromagnetic waves with electric field vectors in the same plane, the beam is said to be plane or linearly polarized. If there are no preferred directions of the electric field vectors when averaged over all electromagnetic waves, the beam is said to be unpolarized. Polarization can therefore be defined as a vector described by its direction and amplitude in an arbitrary coordinate system. A vector rotating with time yields circularly or elliptically polarized light. Some degree of polarization or direction of the electric field oscillation is an optical property inherent in all laser beams [18].

The received lidar signal consist of Rayleigh and vibrational Raman scatter from molecules, and Mie scatter from aerosols and clouds. With the use of spectral filters these scattering components can be separated. Atmospheric scattering occurs as light (e.g. from the laser beam) interacts with a scatter medium (e.g. molecules, aerosols or clouds) in the atmosphere. From Rayleigh scatter molecules scatter the light in all directions, while Mie scatter from clouds and aerosols tends to scatter in a forward direction with regards to incident angle. Rayleigh scatter can be further split into a central Doppler-broadened peak, called the Cabannes line, and sidebands due to rotational Raman scattering. In a high-density gas or condenced matter, the Cabannes line splits to a triplet due to entropy (narrow

central peak) and pressure (Brillouin Stokes and anti-Stokes lines) fluctuations. Literature incorrectly use a wide range of terminology for these processes, such as Rayleigh-Brillouin spectrum, Doppler shift of Rayleigh spectrum, Rayleigh-wing scattering, etc. This thesis will use the terminology (Rayleigh scatter, Cabannes line, Mie scatter, Raman scatter, Brillouin Stokes and anti-Stokes lines) as first presented. While Raman scatter (vibrational and rotational) can cause inelastic scatter, the Cabannes line and Mie scatter returns are elastic, implying that the wavelength of the incident beam remains unchanged. As wavelength remains unchanged, polarization can used for information gathering [19, 20].

Pioneered from scattering theories some 40 years ago and now well established within lidar research is the fact that homogeneous spherical particles elastically backscatter electromagnetic radiation. Following this a range of scattering theories correctly predicted that nonspherical or inhomogeneous particles will induce a depolarized component, i.e. polarization change, in the backscatter. The strength of depolarization depends on the amount of particles and complexity of the particles deviation from sperical symetrical shape, as well as the particles size relative to the radiation wavelength. The refractive index also influences the amount of depolarization generated by nonspherical particles. Implying that laser depolarization measurements are essentially confined to particles without overwhelming absorption at the laser wavelength. Depolarization results predominantly from internal reflections [18].

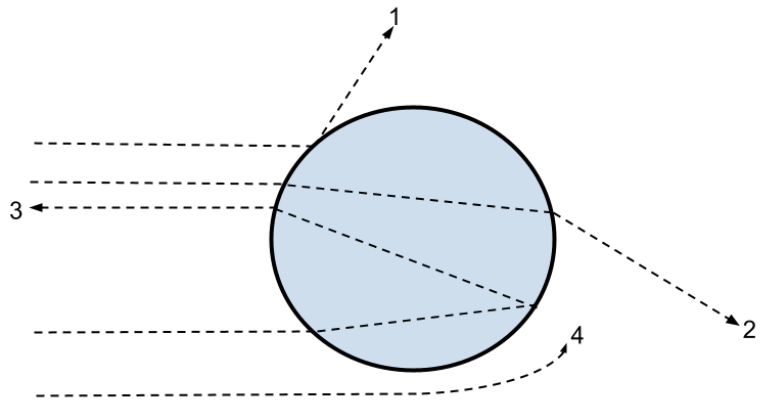

Figure 2.2: Electromagnetic radiation scattering due to particle interaction; 1. reflection, 2. refraction, 3. internal reflection & refraction, 4. diffraction.

Though backscatter occurs primarily from internal reflections & refraction, reflection, refraction and diffraction also cause scatter from interaction with particles. An overview of these scattering processes can be seen in figure 2.2. Aerosol scatter depends on the particles size, morphology, orientation, surface roughness, etc. In addition scattered light from aerosols exhibits polarization features, and the

degree of polarization, as well as the phase function of the polarized component, depend on aerosol type, shape and absorption [21]. Before measures of depolarization can be further discussed a background on the lidar system must be established.

2.3 Troposphere lidar

The ALOMAR observatory have consisted of four different lidar systems. An out of service elastic DIAL O_3 lidar capable of middle atmospheric measurments, an out of service metal resonance Na lidar capable of middle atmospheric measurments, an advanced Rayleigh-Mie-Raman (RMR) lidar for middle atmosphere measurments [22] and a troposphere lidar for low atmospheric measurments .

The troposphere lidar at ALOMAR can be described as an Rayleigh-Mie-Raman lidar and is the classic form of lidar system. The lidar has been operational since 2005 and can dectect Raman, Rayleigh and Mie scatter from the atmosphere. The altitude range is from 0,5 km to 18 km, corresponding to the lowest atmospheric layer, the troposphere. The scope of the thesis is therefore limited by the range of the lidar. A summary of the laser can be found in table 2.1, of note is that ALMOAR only utilize half of the capable altitude range.

Table 2.1: Summary of characteristics for troposphere lidar at ALOMAR.

Specification	ALOMAR
Laser	Quanta Ray Nd:YAG PRO-290
Wavelengths emitted	355 nm, 532 nm, 1064 nm
Pulse energies	375 mJ, 800 mJ, 1600 mJ
Laser power	1020 mJ
Repetition rate	33.333 Hz
Beam divergence	$<$500 μrad
Telescope	Newtonian
Wavelengths detected (elastic)	355 nm, $532_{\parallel}$ nm, $532_{\perp}$ nm, 1064 nm
Wavelengths detected (inelastic)	387 nm, 408 nm, 607 nm, 660 nm
Max signal range	16384 bins
Applied signal range	8192 bins

2.4 The lidar equation

The detected lidar signal can be written as

$$P(R) = KG(R)\beta(R)T(R), \tag{2.1}$$

where P is the received power, R is the distance the from receiver to the scattering region, K is a constant which summarizes the efficiency of the system, $G(R)$ de-

scribes how intensity varies due to changes in the scattering geometry with range. $\beta(R)$ and $T(R)$, the backscatter and transmission coefficients respectively, are atmospheric variables and subject to investigation.

The constant K can be expressed as

$$K = P_0 \frac{c\tau}{2} A\eta, \tag{2.2}$$

where P_0 is the average power and τ is the duration of a single laser pulse. The energy of a single pulse, E_0, can be described by multiplying these two factors, P_0 and τ, together. c is the speed of light, A is the area of the optical receiver, typically a telescope. η is the systems overall efficiency, both for the transmitting and receiving system. The factor $\frac{1}{2}$ is due to backscatter from the leading edge of the laser pulse overlapping with the trailing edge of the laser pulse.

The geometric factor can be described as

$$G(R) = \frac{O(R)}{R^2} \tag{2.3}$$

where $O(R)$ is the laser-beam receiver-field-of-view overlap function. The quadratic decrease in signal intensity with distance is due to the area of the telescope making up part of the scattering volumes surface. This implies that the received signal intensity will equal the true signal intensity when the laser beam and the telescopes field of view overlaps. An example of the effect is shown in figure 2.3. The backscatter coefficient, $\beta(R)$, is highly dependent on the wavelength of the laser and describes how much light is scattered towards the receiver. This is the primary atmospheric parameter that determines the strength of the lidar signal. $\beta(R)$ is determined by the scattering medium,

$$\beta(R,\lambda) = \sum_j N_j(R) \frac{d\sigma}{d\Omega}(\pi,\lambda). \tag{2.4}$$

This is the sum of the concentration of scattering particles, $N_j(R)$, of type j within the volume of the laser pulse, multiplied with the differential backscatter, $\frac{d\sigma}{d\Omega}$, in the backwards direction (π), also known as the backscatter cross section. As the two main contributers to backscatter is molecules and aerosols, $\beta(R,\lambda)$ can be written as,

$$\beta(R,\lambda) = \beta_{mol}(R,\lambda) + \beta_{aer}(R,\lambda). \tag{2.5}$$

Molecular backscatter occurs mainly from interaction with nitrogen (N_2) or oxygen (O_2) molecules. As air density decreases with height, backscatter for ground based systems will decrease with range. Backscatter from aerosols in the atmosphere is highly variable as scatter occurs from a great variety of particles, including, but not limited to, soot, sea-salt, dust, water droplets, ice crystals, sulfates and pollen. The transmission term $T(R)$ accounts for how much light that gets

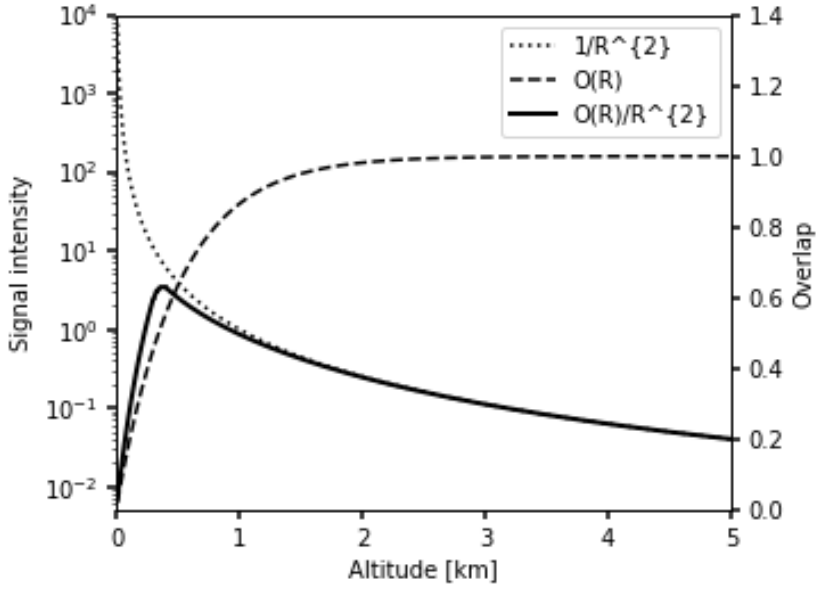

Figure 2.3: Example of the overlap function's effect on received signal, with full overlap at 2 kilometers or with $O(R) = 1$ when $R \geq 2$.

lost on the way to the scatter medium and on the way back [18]. Some literature writes $T^2(R)$ to indicate that one must account for both directions of the light. Here $T(R)$ is defined as

$$T(R,\lambda) = \exp[-2\int_0^R \alpha(r,\lambda)dr] \tag{2.6}$$

where α is the sum of all light extinction coefficients and can be broken down similarly to $\beta(R,\lambda)$,

$$\alpha(R,\lambda) = \sum_j N_j(R)\sigma(\lambda) \tag{2.7}$$

where σ is the extinction cross section for each type of scatter j. Summarizing the individual terms, the lidar equation can now be expressed in the more common form

$$P(R,\lambda) = P_0 \frac{c\tau}{2} A\eta \frac{O(R)}{R^2}\beta(R,\lambda)\exp[-2\int_0^R \alpha(r,\lambda)dr] \tag{2.8}$$

[18].

To determine the transmission coefficient one must know the extinction coefficient. The most common way to determine this would be to use the method de-

veloped by James D. Klett in 1981 [23]. Assuming the backscatter and extinction coefficients are related by some power law of the form

$$\beta = constant \cdot \alpha^k \tag{2.9}$$

where k depends on the lidar wavelength and properties of the atmospheric gases, and introducing the move convenient signal variable

$$S(R) = \ln[r^2 P(R)] \tag{2.10}$$

one ends up with a more well known solution for the extinction coefficient

$$\alpha(R,\lambda) = \frac{\exp[(S - S_m)/k]}{\alpha(R_m,\lambda)^{-1} + \frac{2}{k}\int_r^{r_m} \exp[(S - S_m)/k]dr'} \tag{2.11}$$

where k is assumed to be constant and R_m is chosen as a far distance reference to integrate to, from a distance r. As r decrease from r_m, $\alpha(R,\lambda)$ is determined as the ratio between two progressively larger numbers, providing the advantage that stability and accuracy are easier to maintain [23].

2.5 Measures of Depolarization

For an ideal system the depolarization ratio is given as

$$\delta = \frac{I_\perp}{I_\parallel} \tag{2.12}$$

where $I_\perp$ and $I_\parallel$ are the scattering intensities for perpendicular and parallel polarization channels respectively. Elastic backscatter from a spherical particle will not induce a depolarization component, implying that the backscattered signal from a linearly polarized laser beam will be totally linearly polarized, hence $\delta = 0$. To fulfill this criteria, equation 2.12 must change according to incident polarization. The depolarized component is described by the numerator, thus equation 2.12 describes a system with a parallel polarized incident beam. Particles assumed to be spherical include, but are not limited to wet haze, fog, cloud droplets and small raindrops. If particles are nonspherical the backscattered signal will contain a cross-polarized component, hence $0 < \delta < 1$. Ice crystals, snow flakes and dust are examples of particles causing depolarization of a laser beam [24].

By taking the ratio of the two polarization planes for each laser shot most terms will cancel out leaving the range-resolved linear depolarization ratio, δ, defined as

$$\delta = \left[\frac{\beta_\perp(R)}{\beta_\parallel(R)}\right] \exp(T_\parallel - T_\perp) \tag{2.13}$$

where β and T are the backscatter and transmission coefficients as defined before, separated with respect to the planes of polarization of the laser. In practice the exponential term is not used, but has been historically included to account for the possibility of certain anisotropic targets affecting transmission of light depending on polarization state, an effect well known from microwave radar studies, but not yet established in lidar research. Equation 2.13 is often referred to as the total linear depolarization ratio as it encompasses potential scatter from aerosols, molecules and clouds [18].

Uncertainties in lidar depolarization measurements stem for a range of sources: accounting errors for differences in optical and electronic gain of the channels, poor polarization purity of laser beam, misalignment between polarization plane of laser and detector, just to mention a few. Part of the error can be reduced by a proper design and frequent calibration, but the depolarization ratio should also be corrected,

$$\delta = \left[\frac{P_{\perp}(R)}{P_{\parallel}(R)} \right] C - \chi \tag{2.14}$$

where $P_{\perp}(R)$ and $P_{\parallel}(R)$ are the received powers (or signal strength) for the perpendicular and parallel channel respectively. C is a constant accounting for differences in the detector channels obtained by viewing an unpolarized light source, and χ is a correction term to account for poor laser polarization purity and misalignment of transmitter and detector polarization planes [18]. Extensive research has connected the depolarization ratio to particles in the atmosphere [10–13], but aerosols in particular span a great range of sizes, and spherical particles, such as deliquesced aerosols, produce little to no lidar depolarization. Little depolarization is also expected from strongly absorbing (e.g. carbon-black) aerosols. However the depolarization from inhomogeneous and irregularly shaped aerosols strongly depend on size, and lidar data indicate that for example supermicron-sized desert dust clouds generate δ as large as ~ 0.25 [18].

2.6 Aerosol optical depth and Ångström coefficient

The Beer-Lambert law can be used to measure aerosol concentration, by defining optical depth. Optical depth defines how well photons from the sun are scattered or absorbed by the atmospheric medium. Thus indicating the amount of absorbing gases or particles in the atmosphere. Ångström further built on the Beer-Lambert law by defining optical depth as a function of wavelength with two parameters, turbidity and the Ångström coefficient, providing information about amount and size of particles respectively [25]. Two previous campaigns to characterize particles in the atmosphere above ALOMAR have previously been carried out. These used a sun photometer and/or the troposphere lidar to obtain the Ångström coefficient from the aerosol optical depth (AOD) [26, 27]. AOD was derived from the Beer-Lambert law:

$$F(\lambda) = F_0(\lambda) \cdot \exp[-m(\tau_a + \tau_R + \tau_{O_3})] \tag{2.15}$$

where $F(\lambda)$ is the wavelength dependent signal in mA, $F_0(\lambda)$ is the wavelength dependent instrument signal, m is the airmass factor obtained from a paper by Kasten and Young [28], τ_R is the Rayleigh optical thickness, τ_{O_3} is the ozone optical thickness and τ_a is AOD. AOD was further used to calculate the Ångström coefficient allowing insight to the size of the aerosol, calculated by the formula

$$\tau_a = \beta \cdot \lambda^{-\alpha} \tag{2.16}$$

where β is the turbidity and α is the Ångström coefficient [25]. A drawback with the method implemented in these studies is that the lidar and sun photometer must point in different directions, i.e. away from the sun and into the sun, providing a source of error. Utilizing a study by Miffre *et al.* [14] the polarization of the beam and the wavelength pair 355 nm and 532 nm can be used instead of the sun photometer to further investigate the Ångström coefficient, providing insight to both the particle size and the particle shape without the afford mentioned error.

2.7 The lidar profile

The lidar profile is the received signal frequency plotted against altitude of the scattering signal. The most common way to plot this is with use of semi-logaritmic axes, as with the assumptions of clean air, neglecting geometrical compression and extinction, the signal should only decrease due to changes in pressure. Photons received from scattering in clean air primarily derives from Rayleigh scatter by air molecules and as the atmosphere is expected to become exponentially less dense with altitude, one can expect a straight line on a semi-logarithmic plot. An example of a range corrected signal can be seen in figure 2.4.

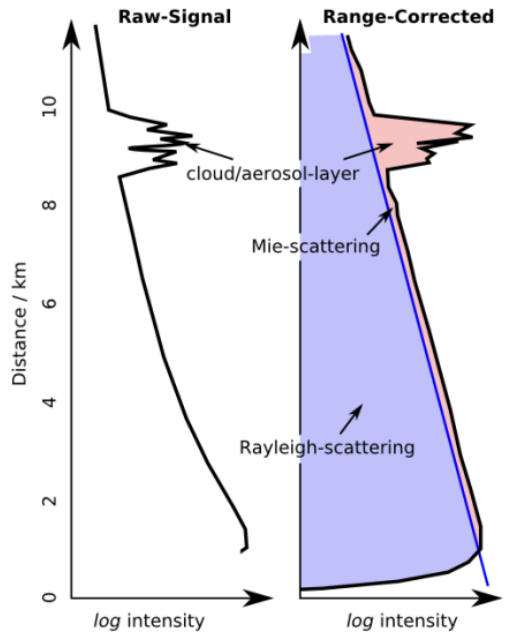

Figure 2.4: Example of raw signal and range corrected signal in thesis by Fimpel [29].

2.8 Polarization filters

When working with polarizing filters the intensity, I, can be calculated based on Malus' Law

$$I = I_0 cos^2\theta \tag{2.17}$$

where θ is the angle between the direction of polarization and the axis of the filter. I and I_0 are the intensities of the transmitted light wave and light wave before the polarizing filter respectively. Working with an unpolarized wave, which can be considered a rapidly varying, random combination of parallel and perpendicular polarizations, the filter will reduce the wave intensity by 50%.

$$I = \frac{1}{2} I_0 \tag{2.18}$$

Malus' law can easily be expanded for two filters, by perceiving I_1 as the source for I_2 and I_1 related to I_0 as in equation 2.17. Hence

$$I_2 = I_1 cos^2\theta_1 = I_0 cos^2\theta_1 cos^2\theta_2 \tag{2.19}$$

where θ_1 is the angle between the direction of polarization of I_0 and the axis of the first filter, while θ_2 is the angle between the direction of polarization of I_1 and the axis of the second filter [30].

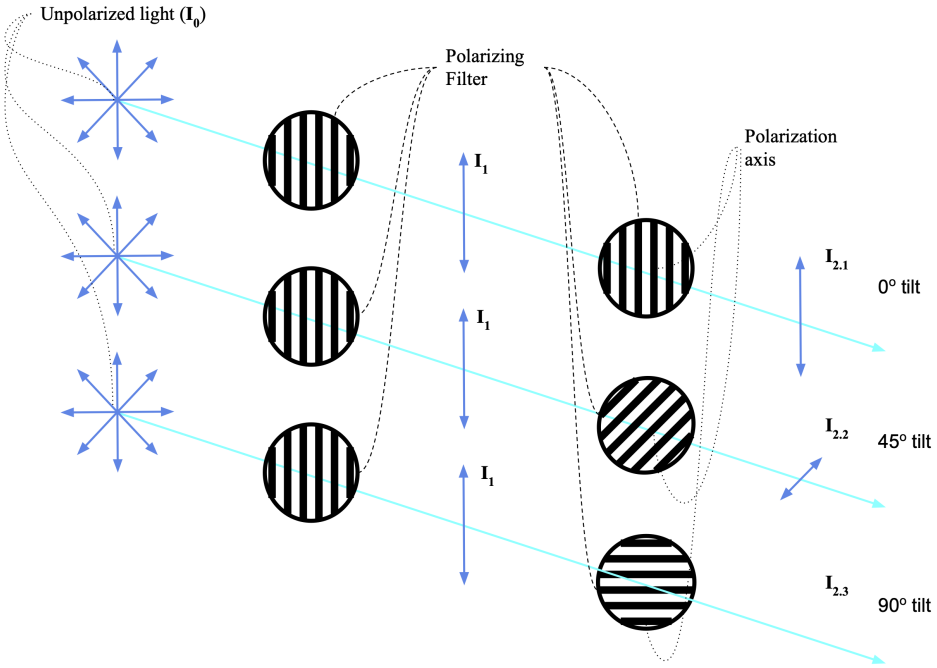

Figure 2.5: Figure showing the effect of two polarizing filters on unpolarized light, with the second filter tilted 0°, 45° and 90° relative to the first filter.

For the three examples in figure 2.5 this gives

$$\begin{aligned} I_{2.1} &= I_1 cos^2\theta_{1.1} = \frac{1}{2} I_0 cos^2 0° = \frac{1}{2} I_0 \\ I_{2.2} &= I_1 cos^2\theta_{1.2} = \frac{1}{2} I_0 cos^2 45° = \frac{1}{4} I_0 \\ I_{2.3} &= I_1 cos^2\theta_{1.3} = \frac{1}{2} I_0 cos^2 90° = 0 \end{aligned} \tag{2.20}$$

Looking at figure 2.6, light passes through the bottom position of the filter wheel, thus implying that the filters must be aligned with their respective axis in the bottom position as they'll rotate while moving to the bottom position.

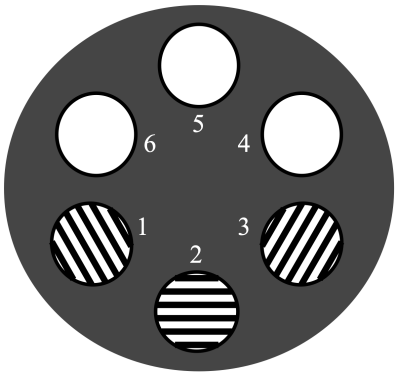

Figure 2.6: Sketch of rotational component of the FW102C filter wheel. Light passes through the bottom position, in this schematic numbered 2.

Figure 2.5 gives and indication to the intended calibration approach. By utilizing that a minimum should occur as the second filter is perpendicular to the first filter, one can determine how accurate the filter wheel calibration is with a secondary rotational filter, seen in figure 2.7.

Figure 2.7: Manual rotational filter used with an attached thin film polarizer to calibrate the motorized filter wheel.

By placing the manual rotational filter in front of the motorized filter wheel the minimum can be found. This implies that the minimum for the second filter, position 3 in figure 2.6, should be a 90 degree rotation on the manual rotational filter from the minimum of the first filter, position 1 in figure 2.6. Using this approach deviation of the filter alignment can be measured.

2.9 Calibration theory

A common lidar system such as the ALOMAR troposhpere lidar can be described grouping individual parts in modules, which in turn are describable by the Stokes-Müller formalism. This formalism is convenient for optical systems as it describes the linear transformation of an elliptically polarized beam, which includes the range from linear to circular polarization, by scattering or passage through a polarizing medium. Briefly, the beam itself is characterized by a Stokes vector, $\boldsymbol{I}$, consisting of four components describing the intensity, ellipticity and orientation of the major axis relative to the scattering plane. The optical system is described by 16 coefficients expressed in terms of the scattering angle and azimuth relative to incident beam, collected in a 4x4 Mueller matrix that linearly transforms the state of polarization of the beam, $\boldsymbol{I}$, after passage through the system [31]. In Stokes-Müller formalism symbols for matrices are bold ($\mathbf{M}$), vectors bold and italic ($\boldsymbol{I}$) and variables italic (I). The setup in figure 2.8, for simplicity not including the 532 nm and 607-1024 nm channels, can be described as

$$\boldsymbol{I}_{T,R} = \eta_{T,R}\mathbf{M}_{T,R}\mathbf{C}\mathbf{M}_O\mathbf{F}\mathbf{M}_E\boldsymbol{I}_L \tag{2.21}$$

where $\mathbf{M}_T$ and $\mathbf{M}_R$ are the Müller matrices for the transmitted and reflected path after the calibrator, $\mathbf{C}$, and $\eta_{T,R}$ their opto-electronic gains respectively. Correspondingly $\boldsymbol{I}_T$ and $\boldsymbol{I}_R$ are the stokes vectors for the electronic signal in the transmitted and the reflected path. $\boldsymbol{I}_L$ is the Stokes vector for the laser beam expanded and directed towards the atmosphere with the backscatter matrix, $\mathbf{F}$. Appropriately $\mathbf{M}_E$ and $\mathbf{M}_O$ are the Müller matrices for the emitter and receiver modules.

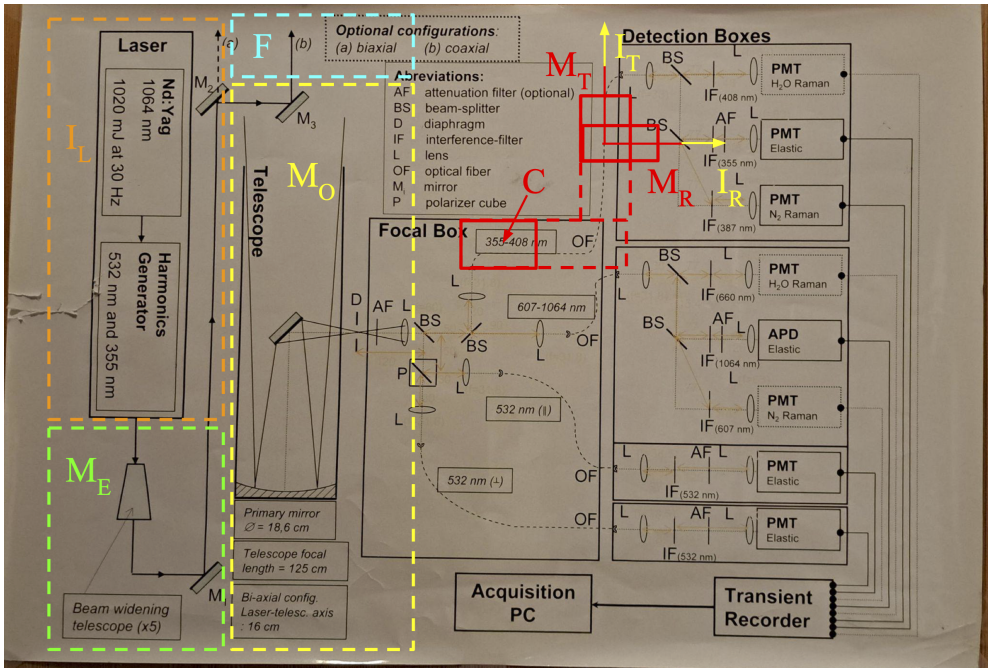

Figure 2.8: Troposphere Lidar schematic subdivided in functional blocks describable by the Stokes-Müller formalism: $\boldsymbol{I}_L$ is the Stokes vector of the laser source, $\mathbf{M}_E$ the Müller matrix of the transmitter optics, $\mathbf{F}$ the atmospheric backscattering volume, $\mathbf{M}_O$ the receiver optics inbefore the calibrator, $\mathbf{C}$, and $\mathbf{M}_{T,R}$ the beamsplitter cube including optics for the transmitted (T) and reflected (R) branches, $\boldsymbol{I}_T$ and $\boldsymbol{I}_R$ being the electronic signals for those respective branches.

The advantage of this formalism is that it can easily account for changes in the system. For example, if the calibration device, C, is placed before the receiver optics rather than the polarizing beam splitter, equation 2.21 simply becomes

$$\boldsymbol{I}_{T,R} = \eta_{T,R}\mathbf{M}_{T,R}\mathbf{M}_O\mathbf{C}\mathbf{F}\mathbf{M}_E\boldsymbol{I}_L \tag{2.22}$$

For simplicity we'll neglect polarizing effects of the receiver optics, $\mathbf{M}_O$, and the laser emitter optics, $\mathbf{M}_E$, simplifying equation 2.21 to

$$\boldsymbol{I}_{T,R} = \eta_{T,R}\mathbf{M}_{T,R}\mathbf{C}\mathbf{F}\boldsymbol{I}_L \tag{2.23}$$

The Stokes vector, $\boldsymbol{I}_L$, is represented by the total power I_L and the state of polarization of horizontally linearly polarized laser light

$$\boldsymbol{I}_L = I_L \begin{pmatrix} 1 \\ 1 \\ 0 \\ 0 \end{pmatrix} \tag{2.24}$$

I_L is the total beam intensity, i.e. the radiant flux or radiant energy per unit of time, not to be confused with the previously defined $P(R)$, the total received power. As

with I_T and I_R, the electronic signals of the detectors in the transmitted and reflected paths, I_L is also directly measurable with a light detector for the flux of photons.

2.9.1 Depolarizing atmospheric aerosol

Before the calibration theory we need to define a few parameters. Müller matrices describe the linear interaction between polarized light and an optical system. Any input in the representation of a Stokes vector will produce an output in the form of another Stokes vector. For the backscattering of randomly oriented, non-spherical particles with rotation and reflection symmetry the Müller matrix **F** can be written as

$$\mathbf{F} = \begin{pmatrix} F_{11} & 0 & 0 & 0 \\ 0 & F_{22} & 0 & 0 \\ 0 & 0 & -F_{22} & 0 \\ 0 & 0 & 0 & F_{44} \end{pmatrix} = F_{11} \begin{pmatrix} 1 & 0 & 0 & 0 \\ 0 & a & 0 & 0 \\ 0 & 0 & -a & 0 \\ 0 & 0 & 0 & 1-2a \end{pmatrix} \tag{2.25}$$

with polarization parameter $a = \frac{F_{22}}{F_{11}}$ and $F_{44} = F_{11} - 2F_{22} = F_{11}(1-2a)$.

In this work the polarization parameter a is defined as the fraction of backscattered light that maintains the emitted linear polarization, and F_{11} as the backscatter coefficient. It should be noted, however, that other definitions can be found in the literature. Equation 2.25 describes a pure depolarizer, including a mirror reflection $\mathbf{M}_M$ for the backscattering direction gives

$$\mathbf{F} = F_{11} \begin{pmatrix} 1 & 0 & 0 & 0 \\ 0 & 1 & 0 & 0 \\ 0 & 0 & -1 & 0 \\ 0 & 0 & 0 & -1 \end{pmatrix} \begin{pmatrix} 1 & 0 & 0 & 0 \\ 0 & a & 0 & 0 \\ 0 & 0 & a & 0 \\ 0 & 0 & 0 & 2a-1 \end{pmatrix} \tag{2.26}$$

The volume linear depolarization ratio δ, described in equation 2.14, of the scatter volume can be written as

$$\delta = \frac{F_{11} - F_{22}}{F_{11} + F_{22}} = \frac{1-a}{1+a} \tag{2.27}$$

implying

$$a = \frac{1-\delta}{1+\delta} \tag{2.28}$$

Horizontally linearly polarized light $\boldsymbol{I}_L$ reflected by the atmosphere **F** and collected in the receiving optics can then be expressed as

$$\boldsymbol{I}_L\mathbf{F} = F_{11}\begin{pmatrix}1 & 0 & 0 & 0\\ 0 & a & 0 & 0\\ 0 & 0 & -a & 0\\ 0 & 0 & 0 & 1-2a\end{pmatrix} I_L \begin{pmatrix}1\\1\\0\\0\end{pmatrix} = F_{11} I_L \begin{pmatrix}1\\a\\0\\0\end{pmatrix} \tag{2.29}$$

2.9.2 Optical parts: diattenuator with retardation

The remaining optical components in the lidar receiver can be described as a combination of diattenuators and retarders, which have two different transmittances for two orthogonal linear polarizations. With many lidar systems, as with this one, a polarizing beam splitter cube is used for separating transmitted and reflected light polarized perpendicular og parallel with respect to the laser polarization. Other systems implement the use of polarizing or non-polarizing beam splitter plates with subsequent polarization filters. All can be described with the Müller matrix of a polarizing beam splitter. The transmitting part as

$$\begin{aligned}\mathbf{M}_T &= \frac{1}{2}\begin{pmatrix} T_T^p + T_T^s & T_T^p - T_T^s & 0 & 0\\ T_T^p - T_T^s & T_T^p + T_T^s & 0 & 0\\ 0 & 0 & 2\sqrt{T_T^p T_T^s}cos\Delta_T & 2\sqrt{T_T^p T_T^s}sin\Delta_T\\ 0 & 0 & -2\sqrt{T_T^p T_T^s}sin\Delta_T & 2\sqrt{T_T^p T_T^s}cos\Delta_T\end{pmatrix}\\ &= T_T\begin{pmatrix}1 & D_T & 0 & 0\\ D_T & 1 & 0 & 0\\ 0 & 0 & Z_T c_T & Z_T s_T\\ 0 & 0 & -Z_T s_T & Z_T c_T\end{pmatrix}\end{aligned} \tag{2.30}$$

with transmission coefficients for parallel polarized (T^p) and perpendicular polarized (T^s) regards the plane of incidence of the polarizing beam splitter. The diattenuation, or property of the transmitting material in which the transmittance depends on the incident polarization state of light, is denoted as D_T. T_T is the average transmittance. Δ_T is the retardance, i.e. the difference in phase shifts of the parallel and perpendicular polarized light.

$$\begin{aligned}&T_T = \frac{T_T^p + T_T^s}{2},\ D_T = \frac{T_T^p - T_T^s}{T_T^p + T_T^s},\ Z_T = \frac{2\sqrt{T_T^p T_T^s}}{T_T^p + T_T^s} = \sqrt{1-D_T^2},\\ &c_T = cos\Delta_T,\ s_T = sin\Delta_T,\ \Delta_T = \phi_T^p - \phi_T^s\end{aligned} \tag{2.31}$$

To simplify we combine subscript for transmitting $_T$ and reflecting $_R$ to splitter $_S$ when appropriate, implying

$$D_S \in \{D_R, D_T\},\ \mathbf{M}_S \in \{\mathbf{M}_R, \mathbf{M}_T\},\ I_S \in \{I_R, I_T\} \tag{2.32}$$

Important not to confuse the notation for splitter, $_S$, with the notation for perpendicular polarized light, ^{s}.

2.9.3 Calibration, depolarization ratio and total signal

Finally reaching calibration theory, still neglecting receiver optics, $\mathbf{M}_O$, with the new splitter subscript and removing the calibrator, i.e. $\mathbf{C} = 1 =$ identity matrix, equation 2.23 represents the standard measurement at the axial rotation of 0°

$$\begin{aligned} \boldsymbol{I}_S(0^\circ) &= \eta_S \mathbf{M}_S \mathbf{F} \boldsymbol{I}_L \\ &= \eta_S T_S \begin{pmatrix} 1 & D_S & 0 & 0 \\ D_S & 1 & 0 & 0 \\ 0 & 0 & Z_S c_S & Z_S s_S \\ 0 & 0 & -Z_S s_S & Z_S c_S \end{pmatrix} F_{11} I_L \begin{pmatrix} 1 \\ a \\ 0 \\ 0 \end{pmatrix} \\ &= \eta_S T_S F_{11} I_L \begin{pmatrix} 1 + D_S a \\ D_S + a \\ 0 \\ 0 \end{pmatrix} \end{aligned} \tag{2.33}$$

The measured signals $I_S(0^\circ)$ are

$$I_S(0^\circ) = \eta_S T_S F_{11} I_L (1 + D_S a) \tag{2.34}$$

Thus it can easily be shown that the ratio of the measured reflected to the transmitted signals is

$$\frac{I_R}{I_T}(0^\circ) = \frac{\eta_R T_R (1 + D_S a)}{\eta_T T_T (1 + D_S a)} = \frac{\eta_R (T_R^p + T_R^s \delta)}{\eta_T (T_T^p + T_T^s \delta)} \tag{2.35}$$

and solvable for δ if the calibration factor, η,

$$\eta \equiv \frac{\eta_R T_R}{\eta_T T_T} \tag{2.36}$$

(with reflectance, T_R, and transmission, T_T, for unpolarized light),the transmission parameters, and the correction for unwanted interference or crosstalk, T_R^p, T_R^s, T_T^p and T_R^s, of the polarizing beam splitter is known. η could also be calculated from equation 2.35 with measurements from unpolarized light, i.e. $a = 0$. Or, as this thesis intends to, determine it by means of calibration measurements. One such method is by rotating the polarizing beam splitter including the detectors by ±45° with regards to the optical axis.

$$
\begin{aligned}
\boldsymbol{I}_S(\pm 45^\circ) &= \eta_S \mathbf{M}_S \mathbf{R}(\pm 45^\circ)\mathbf{F}\boldsymbol{I}_L \\
&= \eta_S \mathbf{M}_S \begin{pmatrix} 1 & 0 & 0 & 0 \\ 0 & 0 & \mp 1 & 0 \\ 0 & \pm 1 & 0 & 0 \\ 0 & 0 & 0 & 1 \end{pmatrix} F_{11} I_L \begin{pmatrix} 1 \\ a \\ 0 \\ 0 \end{pmatrix} \\
&= \eta_S T_S \begin{pmatrix} 1 & D_S & 0 & 0 \\ D_S & 1 & 0 & 0 \\ 0 & 0 & Z_S c_S & Z_S s_S \\ 0 & 0 & -Z_S s_S & Z_S c_S \end{pmatrix} F_{11} I_L \begin{pmatrix} 1 \\ 0 \\ \pm a \\ 0 \end{pmatrix} \\
&= \eta_S T_S F_{11} I_L \begin{pmatrix} 1 \\ D_S \\ \pm a Z_S c_S \\ \mp a Z_S s_S \end{pmatrix}
\end{aligned}
\tag{2.37}
$$

By rotating ±45° the intent is to produce equal light intensities in the transmitted and reflected paths, independent of the atmospheric depolarisation. One issue with this calibration method is the error induced by an potential inaccurate ±45° alignment [32]. The error propagation following an inaccurate alignment has been simulated in a paper by Zhao *et al.*, concluding that a deviation in angle smaller than 5° results in a relative error on the gain ratio of less than 2,7%, but increases sharply above 5° [33].

The measured signal is now

$$I_S(\pm 45^\circ) = \eta_S T_S F_{11} I_L \tag{2.38}$$

and the calibration factor, η, determined from the signal ratio

$$\frac{I_R}{I_T}(\pm 45^\circ) = \frac{\eta_R T_R}{\eta_T T_T} = \eta \tag{2.39}$$

With the calibration factor known, the measured signal ratio δ^* is defined as

$$\delta^* \equiv \frac{1}{\eta}\frac{I_R}{I_T}(0^\circ) = \frac{I_T}{I_R}(\pm 45^\circ)\frac{I_R}{I_T}(0^\circ) = \frac{T_T(T_R^p + T_R^s\delta)}{T_R(T_T^p + T_T^s\delta)} \tag{2.40}$$

which is almost equal to the linear depolarisation ratio, δ, but includes diattenuaton and crosstalk due to an imperfect polarizing beam splitter. The linear depolaristation ratio can now be expressed as

$$\delta = \frac{\delta^* T_R T_T^p - T_T T_R^p}{T_T T_R^s - \delta^* T_R T_T^s} \tag{2.41}$$

Assuming a good polerizing beam splitter the transmitted polarization should contain very little crosstalk, such that

$$T_T^s \ll 1 \implies \{T_R^s \approx 1,\ T_T \approx 0.5T_T^p,\ T_R \approx 0.5(1+T_R^p)\} \tag{2.42}$$

further implying the approximation

$$\delta \approx \delta^* - T_R^p(1-\delta^*) \tag{2.43}$$

The total lidar backscatter signal from the two signals I_T and I_R measured at 0° can now be determined. This is the range-dependent signal, which was used for the inversion of the backscatter coefficient, F_{11}, with lidar inversion methods. From equation 2.34

$$F_{11} = \frac{I_S(0°)}{\eta_S T_S I_L(1+D_S a)} \tag{2.44}$$

Further the polarisation parameter can be extracted from equation 2.35

$$a = \frac{\eta I_T - I_R}{I_R D_T - \eta I_T D_R} \tag{2.45}$$

Inserting equation 2.45 into equation 2.44 yields

$$I_L F_{11} = \frac{\eta_T T_T D_T I_R - \eta_R T_R D_R I_T}{\eta_T T_T \eta_R T_R (D_T + D_R)} = \frac{1}{D_T - D_R}\left(\frac{D_T I_R}{\eta_R T_R} - \frac{D_R I_T}{\eta_T T_T}\right) \tag{2.46}$$

From equation 2.46 the absolute backscatter coefficient, F_{11}, cannot be determined without calibration of the individual channel gains, η_R and η_T, and knowledge of the laser intensity, I_L. However, lidar signal inversions use a reference value at a certain range, which implies only a relative, range-dependent F_{11} is needed. Hence F_{11} can be expressed proportionally as

$$F_{11} \propto D_T I_R - \eta D_R I_T = \frac{T_T^p - T_T^s}{T_T^p + T_T^s} I_R - \eta \frac{T_R^p - T_R^s}{T_R^p + T_R^s} I_T \tag{2.47}$$

Assuming an ideal polarizing beam splitter, i.e. $T_T^p = T_R^s = 1$, $T_R^p = T_T^s = 0$, and thus $D_R =$ -1 and $D_T = 1$, equation 2.47 simplifies to

$$F_{11} \propto I_R - \eta I_T \tag{2.48}$$

as expected. Bearing in mind that in general $T_R^s > T_T^p$, and therefore $(T_R^p - T_R^s) < 0$ and $D_R < 0$, while for the 355 nm and 532 nm depolarization channels at ALOMAR the perpendicular polarization is transmitted and the parallel polarization reflected.

Summarizing, the calibration factor, η, must be determined and the crosstalk corrected for. The linear depolarization ratio, δ, is retrieved from two signals at 0 degrees represented by δ^* in equation 2.40, plus two signals for the calibration factor at ±45 degrees, equation 2.39, and knowledge of the polarizing beam splitter parameters T_R^s, T_R^p, T_T^s and T_T^p for correction of the crosstalk [32].

Chapter 3

Optical setup

Per today the UV channel at ALOMAR only consists of a beamsplitter filtering out wavelengths less than 400 nm to a fiber, used for elastic and inelastic backscatter measurements [9]. An optical setup for a 355 nm UV depolarization channel is proposed with further description of the individual optical components in the next sections. Assuming the backscattered lightrays from the telescope are collimated, the filtered wavelengths from the laser will first pass a filter wheel used for calibration. Then onto a beamsplitter cube to split the p-polarized (parallel polarized) light from the s-polarized (senkrecht polarized, German for perpendicularly polarized) light. The rays further pass a filter to clean the signal of any unwanted polarizations or wavelengths before being focused to a fiber by a combination of two lenses. The fiber transmits the lightrays to the photomultiplier tubes for data processing. A sketching of the proposed setup can be seen in figure 3.2.

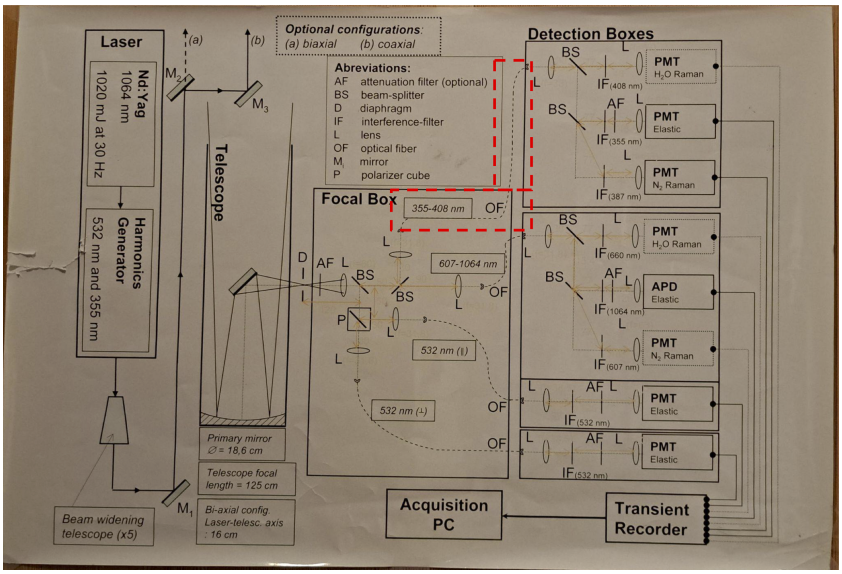

Figure 3.1: Schematic of troposphere lidar system configuration with red outline marking area of implemented depolarization channel.

3.1 Laser - combine with troposphere lidar sub-section?

ALOMAR is outfitted with a Quanta Ray Nd:YAG PRO-290 laser which emits in the infrared spectral region at a wavelength of 1064 nm. Part of the original 1064 nm wavelength is used for frequency doubling and tripling with nonlinear crystals, producing an additional two wavelengths of 532 nm and 355 nm [18]. As seen from table 2.1 the laser power is 1020 mJ at 30 Hz repetition rate. A beam expander is used to keep the laser divergence low, with exit diameter of the laser at 5cm and divergence less than 140μrads. The typical pulse energy for the 355 nm channel is 120 mJ [9]. The manufacturer specifics a polarization "purity" of $>$ 95%, which is not very accurate. Most likely, the laser is much better polarized, but measurement of the polarisation is expensive and it can change during operation or as the laser degrades over time. This is probably why the manufacturer specify a lower limit which they can assure under all circumstances [32]. The laser at ALOMAR is angled such that it produces mainly parallel polarization in the incident beam, thus perpendicular polarization (or the depolarized received beam) will be detected in the transmitted path, further explained in section 3.3. A schematic of the optical setup can be seen in figure 3.2.

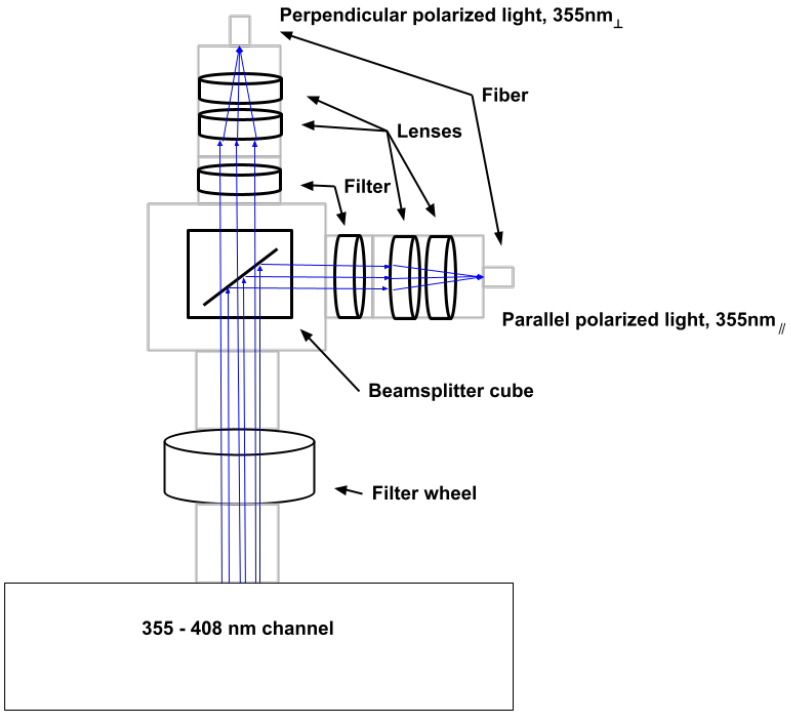

Figure 3.2: Sketched optical setup for the UV 355 nm depolarization channel fitted to the red outline in figure 3.1, with the system mainly in the focal box and the fibers leading to the detection box

3.2 Motorized wheel

The first optomechanical component of the depolarization channel is a filter wheel. The filter wheel will serve as a calibration unit and must consist of minimum four positions,

- filter rotated +45 degrees
- filter rotated 0 degrees
- filter rotated -45 degrees
- open channel for measurements

For calibration the first three positions will be used. By positioning filters rotated 0 degrees and rotated ±45 degrees the calibration method called "±45 degree calibration method" can be employed [32]. The equivalent is used for the pre-existing 532 nm channel and the full method is explained in section 2.9. The advantage of using a motorized filter wheel is full automation of the system, thus limiting time spent adjusting the wheel which is important for the assumption of a constant atmosphere during the operation. The open channel will be used for measurements after the calibration is complete. The FW102C from Thorlabs was selected to solve this task.

3.3 Beamsplitter cube

To seperate the two polarizations of light, a beamsplitter is placed after the filter wheel as indicated in figure 3.2. Apart from splitting the polarizations of the beam, the main important property is high transmission of 355 nm light. Previously described by the manufacturer as the lasers "purity", the polarization extinction ratio (PER) or ratio of p-polarization to s-polarization from the laser is high [34]. The orientation is such that the scattered signal matching the laser polarization is detected as p-polarization, while the weaker depolarized signal is detected as s-polarization. Therefore the beamsplitter cube will be rotated such that s-polarization passes through the cube and p-polarization reflects 90 degrees. This is due to the changing of medium causing part of the light to reflect instead of transmit [35]. By rotating the cube one ensures that the stronger polarization signal will have a minimal contamination from the weaker polarization signal, instead of the opposite. Anti-reflective coating is added to the cube to decrease the reflecting caused by the changing of mediums [36]. The PBS25-355-HP High-Power Polarizing Beamsplitter Cube from Thorlabs was selected for this task.

3.4 Filters

As lidar measurements are based on the backscatter of the laser signal, getting reliable measurements highly depends on transmitting as clean of a signal as possible to the photomultiplier tubes. To ensure the received signal consist of the intended wavelengths, polarization filters are used. Thin film laser line polarizers are

perfect for this, with a transmission of >98% p-polarization [37]. For s-polarized light the filters are rotated 90 degrees with regards to the parallel filter. Hence acting as a filter for s-polarization with equal specifications. The filters are placed before the lenses as indicated in figure 3.2, this is to ensure the light still consist of collimated rays as it passes the filters. An important factor, as varying the incident angle of the rays will shift the filters to a shorter wavelength. Varying temperature will provide a similar effect, with filter wavelength linearly depending on filter temperature [38]. With this in mind it is important to avoid any unnecessary angling of the beam, as well as avoid temperature build up due to light absorption. The thin film laser line polarizers will serve both in calibration with the filter wheel and as filters for any contamination of wavelength or polarization after the beamsplitter cube. 355nm, 25mm diameter, thin film laser line polarizers from Edmund optics are optimal for this task.

3.5 Lenses

Lenses in optical systems should ideally focus one point from the object plane to one point on the image plane exactly. Unfortunately a common problem are chromatic aberrations, meaning the focal length of a lens will shift in accordance with the lights wavelength [39]. A common approximate solution for this is the use of multi-lens systems or achromatic doublets or triplets [40]. As this system ideally consists of a single wavelength, chromatic aberrations should be close to negligible. However, optical components are not perfect and rather than a single wavelength, the system will likely consist of a short interval of wavelengths centered around 355 nm. To counteract any abbreviations a short interval might cause, a convex and a concave lens in succession will be used. Essentially working in a similar fashion to a achromatic doublet, by placing a stronger (shorter focal length) convex lens before a concave lens as indicated in figure 3.3.

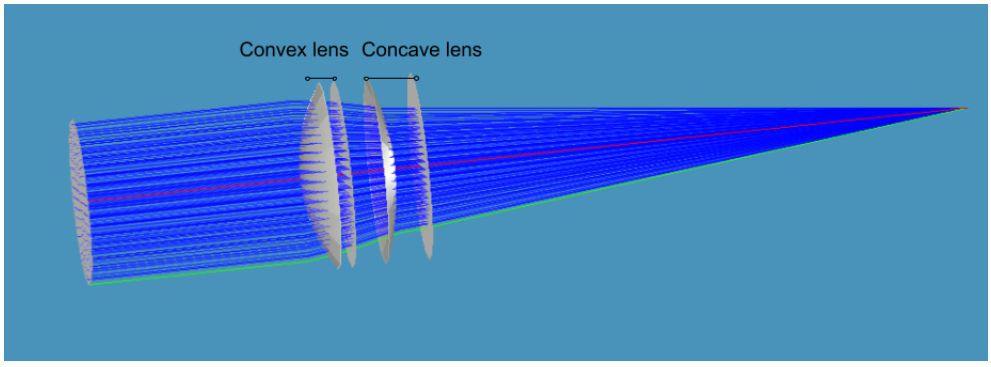

Figure 3.3: Raytrace using Lensforge of Thorlabs LA4148 (convex lens) and LC4513 (concave lens). Simulating with 200 collimated rays and 7mm distance between the lenses. Marginal ray and Chief ray in green and red respectivly

3.6 Fibers

A fiber will be placed in the focus of the lenses. As the lens tubes have a diameter of 25 mm and the fiber has a diameter of 2.3 μm, the absolute value of the magnification must be ≤ 0.000092. This is only if the backscattered beam used the full diameter of the Thorlabs lens tubes, which is not the case as that would cause light to scatter of the internal components (lens tube walls, retaining rings, etc.). Thus this magnification is not absolute, but a good basis for initial computations. Important to note is the potential change in polarization caused by the fiber and for this reason a polarization maintaining (PM) fiber will be used. As the fibers are placed after the beamsplitter cube, this is not a concern for this design, but PM fibers will still be used as they are more flexible to design changes. To limit loss in fibers, as short a fiber as possible should be implemented, as well as avoiding any excessive bending of the fiber. Another important note is the angle of the fibers acceptance range, implying that rays with angle of incidence to large will not be accepted. Thorlabs describes their fibers with the property numerical aperture (NA). NA is a measurement of the opical fibers ability to capture light. From Thorlabs website the fiber PM-S350-HP has NA $= 0.12$ [41]. Numerical aperture can be described as

$$NA = n\sin(\theta) \tag{3.1}$$

where θ is the half cone angle and n is the index of refraction [42]. n is approximately equal to one for air. With the thin lens approximation, n is about one for the lens system. Hence the sine of half the acceptance angle is equal to NA. With the previously described two lens setup and a distance of 7mm between the lenses, a 6,86° maximum angle of incidence from the principal axis will be transmitted to the fiber, just below the fibers acceptance range of 6,89°. Decreasing the distance between the lenses increases the combined focal length, which in turn decreases the maximum incident angle. The lenses LA4148 and LC4513 with a maximum of 7mm distance in combination with Thorlabs PM-S350-HP fiber are selected for this system.

3.7 Summary of optical components

The optical components have been chosen based on three main properties; performance, cost and weight. During the construction of the 532 nm depolarization system Thorlabs one inch components where exclusively used, meaning the UV channel per today also has a one inch tube mount. As mounting the proposed system to the preexisting system is unavoidable, a fourth requirement of all components being compatible with Thorlabs 1 inch components where made. A summary of the selected components can be found below.

Table 3.1: Summary of optical components

Optical component	Product name	Amount	Distributor
Filter wheel	FW102C	1	Thorlabs
Beamsplitter cube	PBS25-355-HP	1	Thorlabs
Filter	#86-707	4	Edmund Optics
Convex lens	LA4148	2	Thorlabs
Concave lens	LC4513	2	Thorlabs
Fiber	PM-S350-HP	2	Thorlabs

Chapter 4

Data processing

Before analyzing the lidar profile the raw signal data must be processed. ALOMAR use Licel transient recorders for data processing. The Licel software use range bins instead of km for altitude measurements. Range bins , commonly called resolution steps (dR), can be determined by

$$dR = \frac{c\tau}{2} \tag{4.1}$$

where c is the speed of light, τ is as defined earlier the pulse duration and the factor $1/2$ is due to the light traveling both ways in the resolution step [43]. Knowing the sampling frequency is 20 MHz, the pulse duration must be $\frac{1}{20\,\text{MHz}} = 50$ ns. Following, the range bins are quickly calculated to 7.5 m with equation 4.1. Thus from table 2.1 the max and applied signal ranges become 122800 m and 61440 m respectively.

4.1 Photomultiplier tubes

Licel transient recorders process signals from electrical currents, implying that the often weak backscattered signal from the atmosphere must be amplified. For this, Photomultiplier tubes (PMTs) are used. A PMT is an electron tube composed of a photocathode coated with a photosensitive material. Signal reaching the cathode causes the release of electrons into the tube thought the photoelectric effect. These electrons are attracted to and accelerated towards the first positively charged dynode. Several dynodes are arranged such that electrons from each dynode are directed towards the next dynode in a series. Electrons emitted from each dynode are accelerated by the applied voltage towards the next dynode, where their impact causes the emission of numerous secondary electrons. These electrons are also accelerated to the next dynode, thus generating a cascade of electrons. At the last dynode the stream of electrons are accelerated to the anode and produce a current pulse in the load resistor, representing an external circuit. This current is the current registered in Licel transient recorders and is proportional to the intensity

of the signal reaching the cathode. In a well designed PMT emitted photoelectrons can produce between one and eight secondary electrons at each dynode impact. A PMT is used as it is capable of detecting extremely low intensity levels of light, even individual photons [44].

When the electrical current from the PMTs reach the Licel transient recorder, the signal is ready to be processed. The data processing can be summarized in six steps. For all corrections the measurement uncertainty is considered and combined using the standard Gaussian error propagation.

4.2 Dead-time correction

Licel photon counters in general have certain limitations during photon counting. Dead-time is defined as the minimum time needed for the photon counter to distinguish between two photons. Due to the electron cascade, the pulse at the anode has a width. Should two photons hit simultaneously, these pulses will overlap. Normally counters are rated according to their ability to count "clock" pulses (regular spacing). However, the photons come at random times (in a Poisson distribution), so that some are too close to distinguish. A general rule of thumb is that a 10 MHz counter will be linear (photons to counts) from the dark count to 1 MHz. As photon scatter from the laser is high, so is the likelihood of missing photons. Photons hitting within the dead-time are simply lost and detector saturation will be reached proportionally to the inverse of dead-time. As this is a statistical problem and the system can be described as non-paralyzable, the count rate is given as

$$S = \frac{N}{1 - N \cdot \tau_d} \tag{4.2}$$

Where S is the true count rate, N is the observed count rate, and τ_d is the system dead time. This is a theoretical model and only valid if $N < \tau d$ [45]. Implying that the model is good as long as the observed count rate per dead-time is less than one on average.

4.3 Background correction

The detected lidar signal will always consist of some background noise or undesired signal. At daytime, the background signal consist mostly of direct or scattered sunlight, while nighttime is dominated by the moon, stars and artificial light sources. All these factors must be accounted for before a lidar signal can be evaluated further [18]. In the raw signal this can be seen at great heights, where the atmospheric scattering is negligible, and between shots where the observed count rate becomes close to constant. The average of this observed constant is subtracted from the signal. Note that this also accounts for the dark count, which arises

from thermal generation of electrons from the cathode.

4.4 Range correction

Range correction is a widely used approach as it does not require the use of reflectance targets, as it would be nearly impossible for non-stationary lidars. The correction is based on a simplified form of the radar equation, which normalizes intensities for a range with respect to a reference range as

$$I_{corrected} = \left(\frac{R}{R_{reference}} \right)^{f} \cdot I_{original} \tag{4.3}$$

where I is the corrected and original intensities respectively, R is the distance from the lidar to the scatter source, $R_{reference}$ is the mean distance and f is the tuning parameter. Theory suggests that f cannot be smaller than 2.0 [46]. Implying that the received signal will decrease with height proportional to the factor $\frac{1}{R^2}$. Similar to the previously described overlap function in equation 2.3, correction for this is known as the range correction.

4.5 Bin shift correction

The photomultipliers used measure in both discrete photon counting and analog mode. For high intensity light, the photon count is high, implying that the analog signal or the mean of the current observed is used. While for low intensity light the current pulses can be counted individually, implying discrete photon counting. The analog and the photoncounting data has a fixed shift between them due to two factors. Firstly analog bandwith, the preamplifier contains a antialias filter with a bandpass of half the sampling frequency, delaying the analog signal by two bins compared to the photon counting. Secondly the Analog-to-Digital Converter (ADC) sample voltage in a multiple step process, implying that the sample result is available several clock cycles after the actual sampling took place [47]. The bin shift correction between analog mode and photon counting at ALOMAR is three bins.

4.6 Zero-bin correction

Most lidar instruments utilize a trigger to activate the pulse-firing from the transmitter and data acquisition in the receiver. Even so a temporal delay between the activations may occur. This creates a spatial displacement in the received signal with respect to the real position of the source. To ensure that the first resolution step, i.e. first bin, is the first altitude measured a zero-bin correction is completed. A common fix is to place a source with known distance from the lidar and measure the backscatter. This will reveal the necessary calibration for the zero-bin.

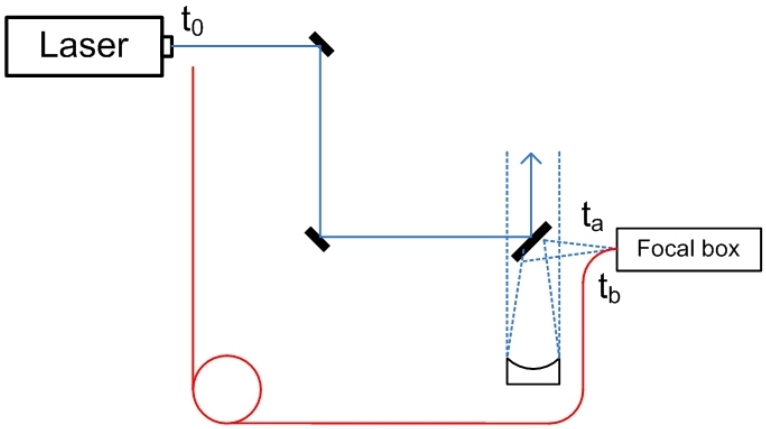

Figure 4.1: Experimental setup used for calculating zero bin correction at ALOMAR. 100 meter fiber with known transmission, t_0 is trigger activation, t_a is time when signal received from first atmospheric backscatter, t_b is time when signal is received from fiber.

A similar approach has been used to calculate the zero bin correction at ALOMAR. Figure 4.1 shows the experimental setup. Using a 100 meter fiber with known transmission and measuring the distance between the laser and the focal box to be 7 meters, the calculation could be made after measuring t_a and t_b. The zero bin correction used at ALOMAR is three bins.

4.7 Gluing

Finally the analog and the discrete photon counting modes can be combined or glued together for a complete lidar profile.

Chapter 5

Experimental setup

Before implementation at ALOMAR it was important to prove that the proposed design would be functional, thus a proof of concept or benchmark test was completed. As there were no available lidar systems in Trondheim to test the depolarization channel on an alternate system was implemented to simulate the backscatter transmitted from the beamsplitter in the focal box, marked as the red outline in figure 3.1. The setup used to simulate the reciver setup at ALOMAR for benchmark tests in Trondheim can be seen in figure 5.1. The fibers where in turn connected a low power detector transmitting the signal to an optical power meter. The detector and power meter can be seen in figure 5.5.

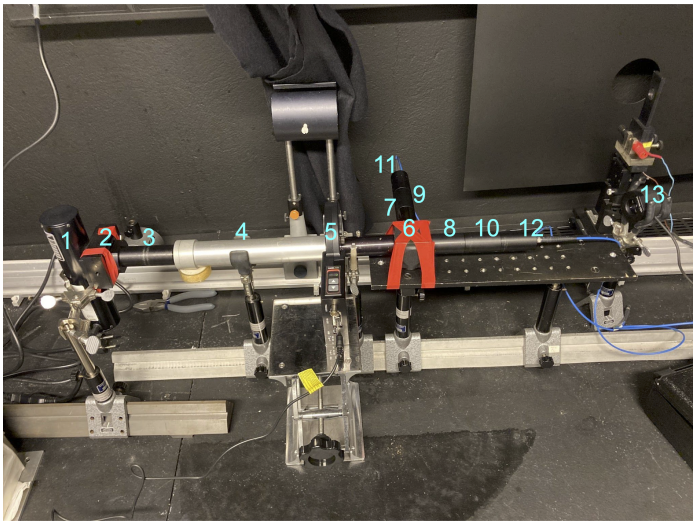

Figure 5.1: Experimental setup; 1. Mercury lamp, 2. Mercury lamp exit slit with adjustable pinhole, 3. Lens tube with biconvex lens and bandpass filter, 4. Sun photometer, 5. Filter wheel, 6. Beamsplitter cube, 7. Filter in parallel channel, 8. Filter in perpendicular channel, 9. Two lens system in parallel channel, 10. Two lens system in perpendicular channel, 11. Fiber in parallel channel, 12. Fiber in perpendicular channel, 13. Newport detector.

5.1 Mercury lamp, pinhole and biconvex lens

The germicidal low pressure mercury lamp has a broad emission spectrum, with peak emissions at 253.65 nm, 296.73 nm, 365.02 nm, 404.66 nm, 365.02 nm, 404.66 nm, 576.96 nm, 579.07 nm [48]. A spectrometer was used to confirm that the mercury lamp exhibited the full spectrum. The pinhole in combination with the mercury lamp acts as a point source, and can be seen in figure 5.2. The pinhole was placed in the focal point of the biconvex lens, with the collimator placed in the other focal point. Thus all light exiting the pinhole should focus to the collimator.

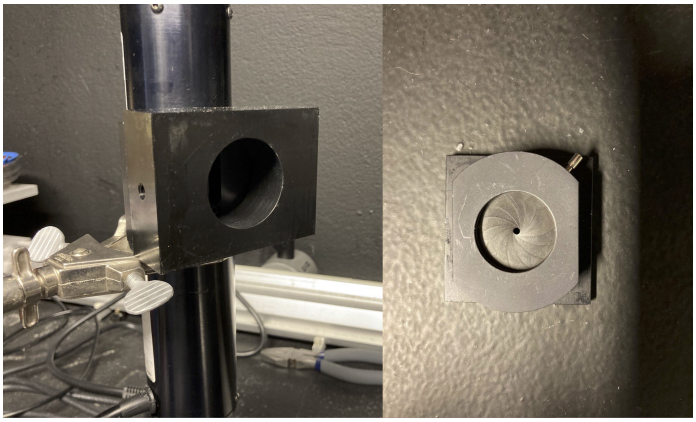

Figure 5.2: To the left a germicidal low pressure mercury lamp and an adjustable pinhole. The pinhole can be seen attached to the lamp in figure 5.1.

5.2 Bandpass filter

Due to the Mercury lamps broad emission spectrum a narrow bandpass filter was implemented to reduce the amount of unwanted wavelengths within the system and thus get a better proof of concept test. Figure 5.3 shows that transmission for the bandpass filter starts at about 340 nm and ends at about 380 nm, perfect for the intended peak emission 365 nm. The disadvantage of this bandpass filter was the low transmission, letting through less than 50% of the desired wavelength.

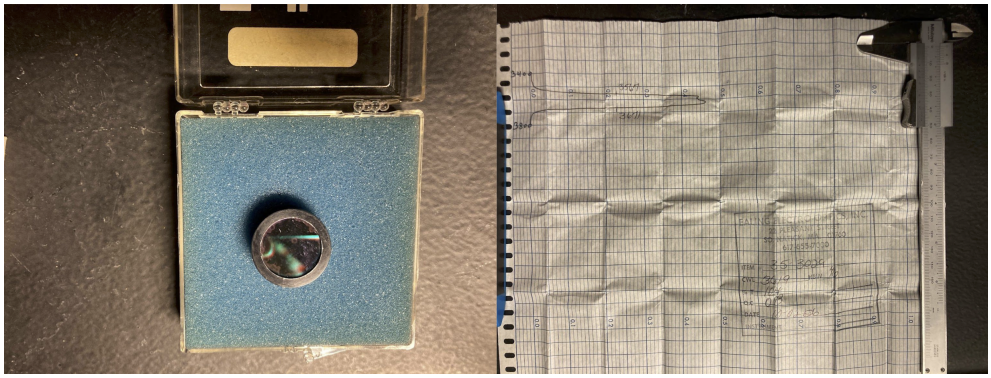

Figure 5.3: To the left the narrow bandpass filter. To the right the narrow bandpass filter transmission curve.

5.3 Collimator

The mercury lamp exhibits uncollimated light. To better simulate the receiver setup at ALOMAR a Sun photometer collimator (J004-SMA), seen in figure 5.4, was implemented in the experimental system to collimate the light traveling through the system. Normally used as a telescope in the study of direct irradiance of the solar radiation, the optic utilized a UV-grade fused-silica window to provide high transmission of UV radiation. As the optic has a field of view of 1.5 degrees, one can feed light from a fiber through the SMA connection and expect reasonably collimated light transmitted to the optical system [49]. As the both the fibers where in use, an alternate solution was used, focusing light from the the pinhole to the SMA entrance with a biconvex lens instead of a fiber.

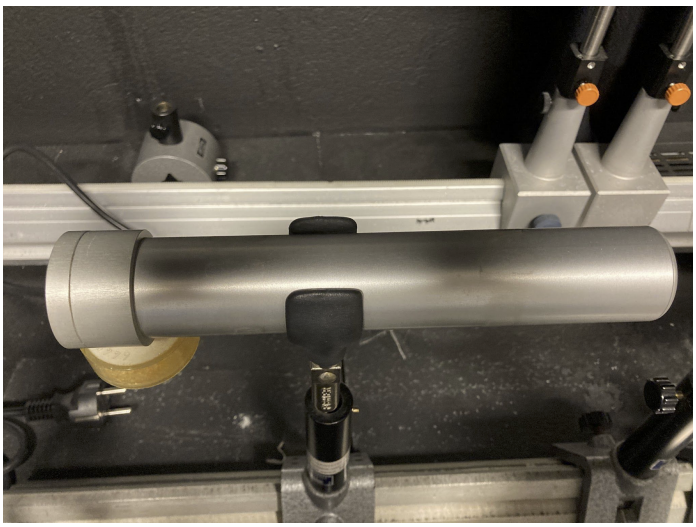

Figure 5.4: A J004-SMA sun photometer collimator. Used in the experimental setup to produce collimated light for the depolarization channel.

5.4 Optical power meter

At ALOMAR photomultiplier tubes in combination with Licel transient recorders are used for processing the signal received from the fiber, as a replacement for the experimental setup a Newport optical power meter and manual recording was used.

Figure 5.5: To the left a Newport 918 low power detector and to the left a Newport 2930C duel channel optical power meter.

5.5 Experimental results

Figure 5.6 shows the signal intensity in the two channels during the mercury lamp warmup phase. As expected the signal rises from low to high during the warmup phase, before stabilizing at about 42 pA and 55 pA in the perpendicular and the parallel channel respectively.

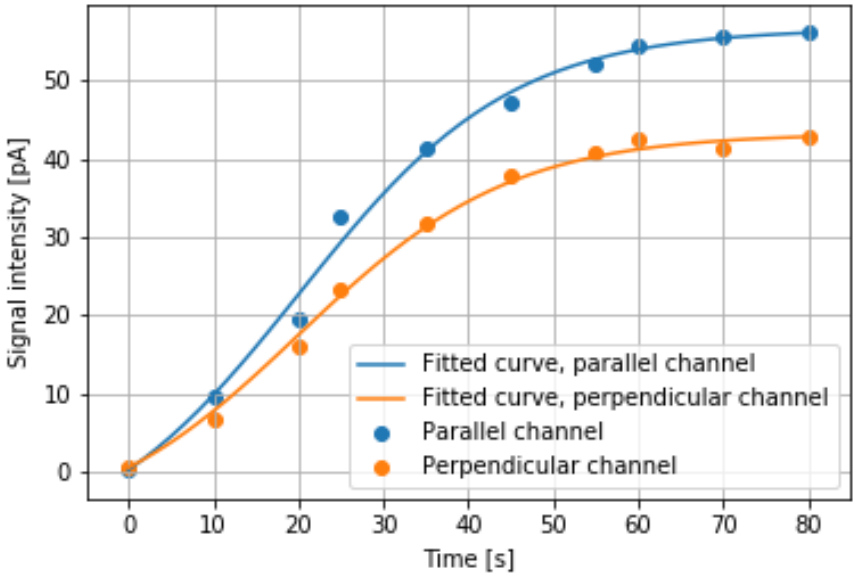

Figure 5.6: Signal intensity through the mercuary lamp warmup phase. Measurements where run with the filterwheel in an open channel. Manual measurement points added with fitted curve.

Notably the results imply that the mercury lamp exhibits a slight preference to parallel polarization. This is unexpected as the mercury lamp should produce unpolarized light, but could be due to internal reflections within the lamp tube and housing, or to slight misalignment of the optical components producing scatter or changes in polarization. Further the signal received is quite weak, only on the scale of picoampere. This could also be due to misalignment, but more likely a combination of the relatively low output from the mercury lamp, a small pinhole drastically reducing the amount of light entering the system, as well as a low transmission through the bandpass filter. These tests where only intended as proof of concept and not as the results themselves, thus optical alignment and high transmission was not prioritized. A performance test was to follow during the implementation at ALOMAR.

5.6 Experimental calibration results

Previously a paper by Zhao *et al.* highlighted the importance of an accurate filter wheel calibration [33]. Following the setup explained in section 2.8, calibration of the filter wheel was completed, yielding the following results.

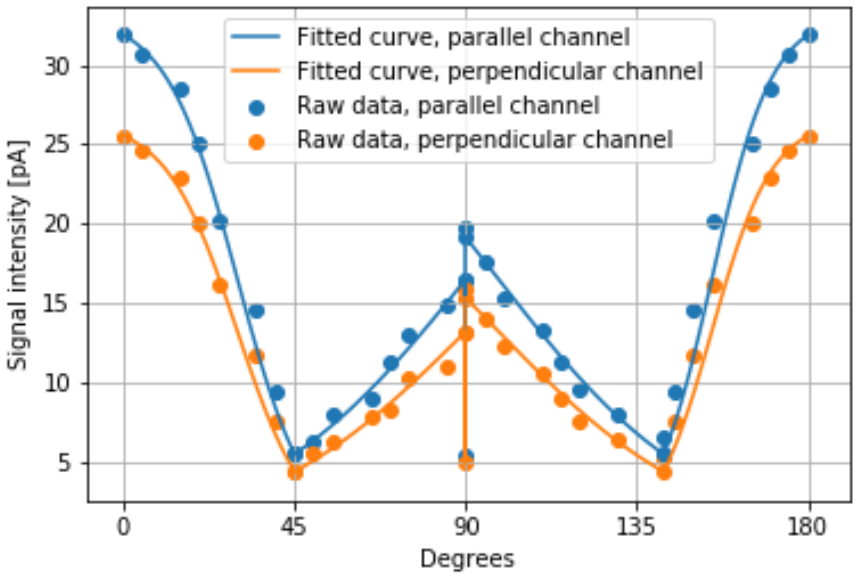

Figure 5.7: Offset filter wheel calibration. Manual measurement points with fitted curve. The drop in signal at 90 degrees is due to switching the motorized filter wheel from position 1 to position 3.

Figure 5.7 shows a slight offset of 6-7 degrees, the minimum of the first filter can be seen at 45 degrees, related to the degrees on the manual rotational filter wheel. Implying that the second filter should have a minimum at 135 degrees. Another indication to the error in figure 5.7 is the offset between filter switches. Utilising that the mercury lamp exhibits unpolarized light and rotating the manual filter wheel 45 degrees after the initial minimum, the output right before and right after switching filter wheel position should be equal due to the alignment of the filters.

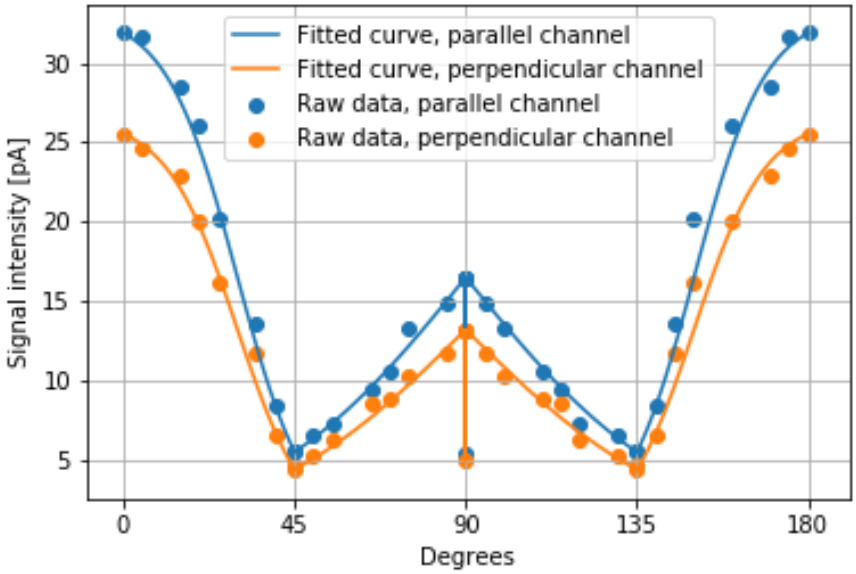

Figure 5.8: Corrected filter wheel calibration. Manual measurement points with fitted curve. The drop in signal at 90 degrees is due to switching the motorized filter wheel from position 1 to position 3.

Figure 5.8 shows the corrected calibration. Notably the minimums are larger than zero signal, implying that the two filters are letting through some light. This is probably due to noise in the system, fibers or low power detector. One cause of noise could be the bandpass filter letting through unintended wavelengths. Light between 340 - 460 nm will be transmitted by the fiber and the longer wavelengths are less affected by the filters compared to the design wavelength and thus create noise. For the ±45 degree method calibration for the filter in position 2 from figure 2.6 should be included to ensure accuracy of filters in position 1 and 3 being ±45 degrees from this filter.

Chapter 6

Implementation at ALOMAR

Due to several shipment delays and malfunctioning equipment, combined with the time constraint of a masters project I was unable to achieve all that I wanted, leaving a good amount for future work.

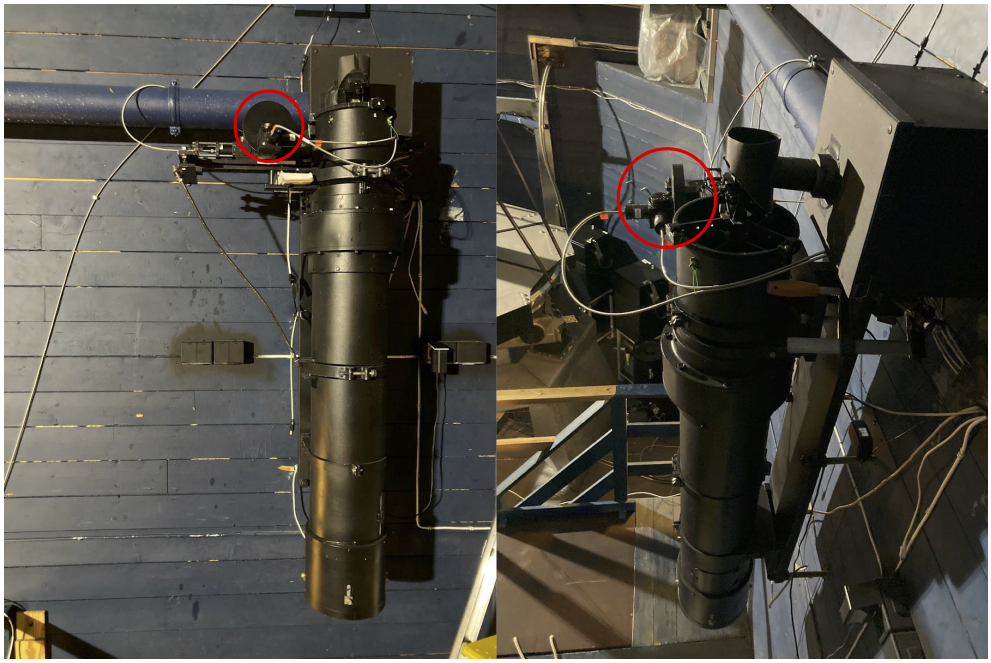

Figure 6.1: Telescope and attached focal box, 532 nm calibration wheel marked with a red circle.

From figure 6.1 the focal box can be seen mounted to the telescope, with the circular calibration wheel for the 532 nm depolarization channel being most recognizable and marked with a red circle. This design necessitates a lengthy re-calibration whenever access to the focal box is required, as the telescope must be disassembled and realigned. Due to the lengthy re-calibration process the planned

and proposed design was rejected while at ALOMAR. An alternate solution was proposed, using the polarization maintaining fibers to transmit 355 nm light to the detection box without changing the polarization. Only changing the fiber leading from the telescope would avoid dismantling the telescope and thus also avoid the re-calibration. The depolarization channel would then be implemented in the detection box, seen in figure 6.2.

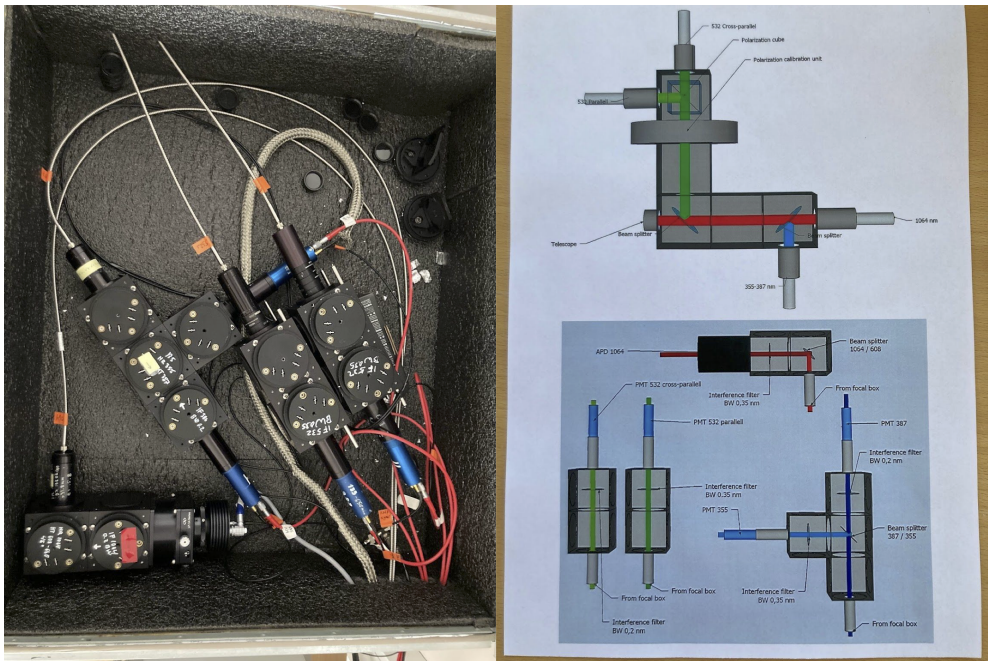

Figure 6.2: Picture and Schematic overview of the detection box.

Advantages of this setup would be easy access to the depolarization channel, allowing for re-calibration, adjustments and the swapping optical components without re-calibrating the telescope. Potential issues are the unknown effect of the polarization maintaining fiber on the polarization, and the premounted lens focusing from the telescope to the fiber either not achieving the necessary magnification with regards to the fiber diameter, or the angle of incidence of the focused light beam being larger than the acceptance angle of the fiber. These latter two would result in either increased scatter or loss of signal, which could limit the range.

Figure 6.3: Picture of troposphere laser.

For the initial issue, fibers effect on polarization, several tests where attempted. First with a 532 nm laser pen, as the 405 nm pen was malfunctioning. The pen would have high collimation, making it excellent for simulating the received laser signal. Thorlabs only specify the lower cutoff for their fibers, so the thought was that transmission for higher wavelengths would be possible, but likely poor [41].

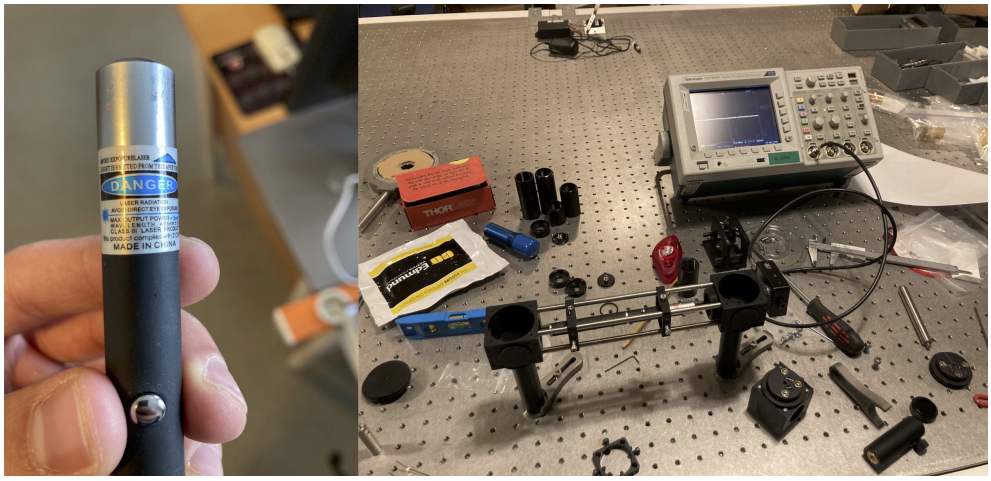

Figure 6.4: On the left the malfunctioning 405 nm laser pen. On the right the laser pen setup for benchmark tests of fiber influence on polarization

Using polarizing filters for 532 nm benchmark tests for the laser pen where run, the results can be seen schematically in table 6.1. Theoretically, with both parallel and perpendicular filter in place, one would expect no signal, but about 10% of light was still transmitted. This is likely due to poor alignment or imperfect filters.

Unfortunately no signal was achieved when the fiber was implemented, and it was later confirmed with a simple mobile phone light test that only blue light transmits through the fiber. The white light from a phone is created by three diodes in red, green and blue wavelengths, thus one can shine light on one end of the fiber and use the naked eye on the other end to see what color the transmitted light is. A likely reason for the upper limit on transmitted wavelength is bend-losses in the fiber, which is higher for longer wavelengths.

Table 6.1: Benchmark tests for 532 nm laser pen.

System components	Output	Output with fiber
Laser pen	20mW	-
w/ parallel filter	5mW	-
w/ perpendicular filter	15 mW	-
w/ parallel and perpendicular filter	2mW	-
w/ perpendicular filter x2	15 mW	-
w/ parallel filter x2	5mW	-

Next a Perkin-Elmer lambda 900 spectrophotometer able to produce wavelengths between 175 nm and 3300 nm, was intended as a light source for the lab tests. Unfortunatly the spectrophotometer produced quite weak and uncollimated light with only a 5% transmission through a normal fiber compared to direct transmission from exit slit to detector slit. The poor transmission combined with a high incidence angle from the preinstalled lenses lead to a signal through the polarization maintaining fiber indistinguishable from background noise. An attempt to collimate and refocus the light was made, but due to the short working distance within the spectrophotometer a fiber to a secondary working station had to be used. The low transmission, even invisible to the naked eye at 532 nm, led to undetectable signal. This was likely due to a combination of a weak signal from the first fiber and some signal lost when collimating and refocusing. The Perkin-Elmer spectrophotometer can be seen in figure 6.5.

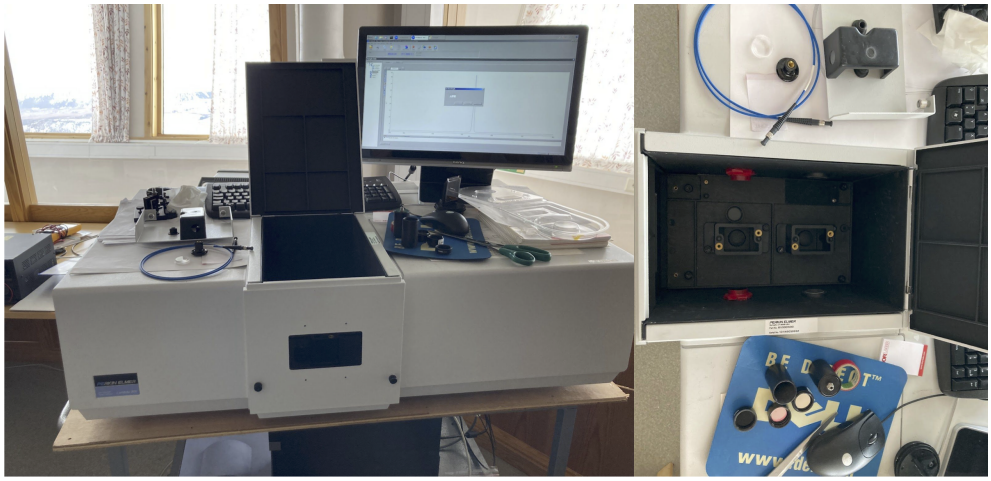

Figure 6.5: Perkin-Elmer lambda 900 spectrophotometer with bird's-eye view of exit and detector slits

Final attempt was to filter out 355 nm light from the troposphere laser itself, seen in figure 6.3. Potential issues with this approach was that the laser intensity would be too strong and damage the optical components, of special concern was the fiber because the entrance diameter requires a strong focus of the already intense beam. To limit the intensity of the beam neutral density filters were installed, leading to another worry. Neutral density filters work by absorbing part of the beam as heat energy. Overheating the density filters would reduce the absorption and potentially still damage the optical components. The test setup can be seen in figure 6.6 and consisted of the laser, the beam expander, two mirrors, two beamsplitters and a detector. Two pinholes and a 1024 nm laser was used for adjusting the beam path, and Thorlabs cubes for reducing the scatter from unused wavelengths. Unfortunately, leading up to my stay at ALOMAR the laser obtained an oscillator issue. It was believed that the faulty oscillator could be remotely started, thus operating the lidar as usual, but when the test setup in figure 6.6 was completed, the remote startup also failed. The laser is per today out of commission and awaiting service.

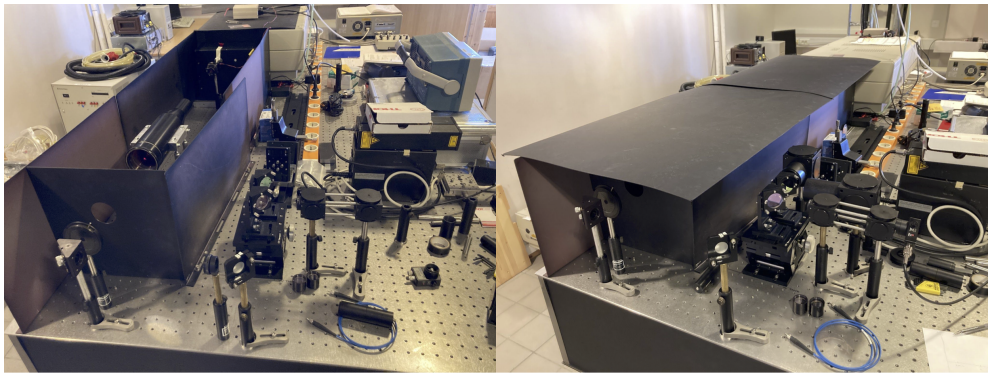

Figure 6.6: On the left the unfinished test setup can be seen, with a 1024 nm laser and two pinholes used for adjusting the mirrors and beam path. On the right the finished test setup can be seen, with cubes for reducing the scatter from the unused wavelengths.

While setup from figure 6.6 was installed, damage on the beam expander entrance and exit lenses was found. The laser last received maintenance in February and have likely been harming the beam expander since. The lens damage can be seen in figure 6.7, showcasing that even if the laser were operating normally the results produced, and calibration based on those results would be speculative at best, due to the changing of polarization caused by the beam expander. Changing the lenses was possible, but without knowing the influence of the potential internal damages of the beam expander, the results would be deemed conjectural.

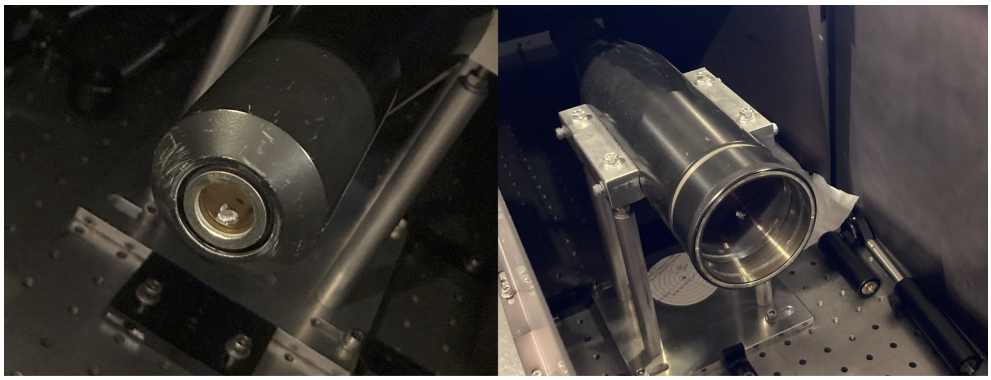

Figure 6.7: Beam expander with damages from the laser beam

When the project was proposed the plan was to install the depolarization channel in the focal box, similar to the 532 nm channel and marked with a red outline in figure 3.1. This would cancel all other channels with wavelengths of the range 355-408 nm, and more specifically the existing 387 nm Raman channel, seen in figure 6.2. During my stay this proved to be undesired after all. An alternative solution, to install the depolarization channel after the 355/387 nm beam splitter was proposed. The issues with this proposed solution is that the 355/387 nm

beam splitter is a dichroic mirror unintended for polarization work, thus causing an unknown polarization on the signal and rendering the results speculative. The effect could be measured or the mirror swapped, but as per today the issue remains unsolved.

6.1 2021 Results

As I was unable to implement the 355 nm depolarization channel at ALOMAR due to problems with the system a short analysis of some existing results are included, with reference to what could be achieved when the laser is operational and the channel installed. ALOMAR uses the previously mentioned ±45 degree calibration method for calibration of the 532 nm channel.

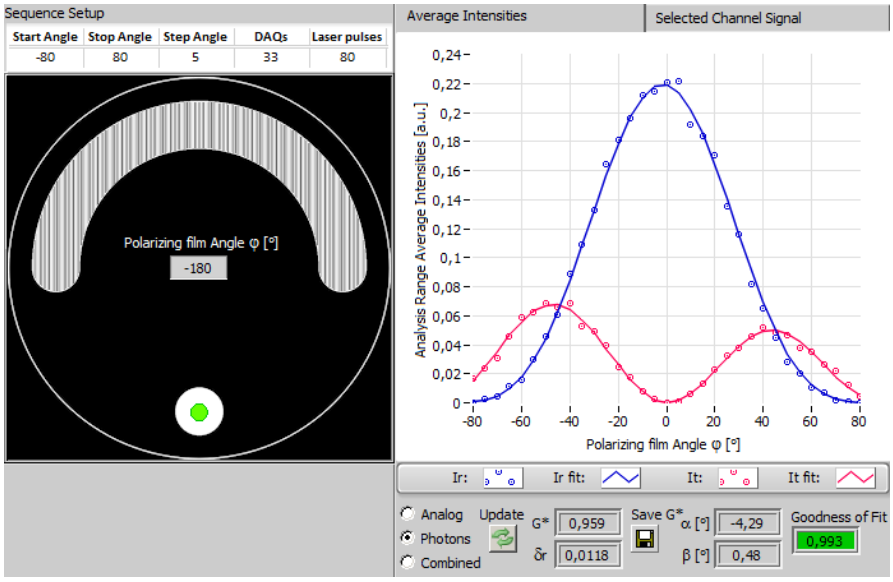

Figure 6.8: Calibration wheel position and calibration measurement from 532 nm channel on 4th of August 2021, plotted with Labview. Reflected(||) channel in blue and transmitted(⊥) channel in red.

Figure 6.8 shows a calibration measurement for the 532 nm depolarization channel. Theoretically the signal intensities at polarizing film angle ±45° should be equal as explained in section 2.9.3. The inequality in combination with the slight shift of the reflected path intensity peak implies a slight rotation of the plane of polarization, a re-calibration of the filter wheel should thus be preformed [29]. Though other calibration techniques exits, the ±45 degree calibration method was the calibration of choice. This was due to simplifying the operational work for the employees at ALOMAR, as both depolarization channels would be based on the same calibration technique. There would still be differences, the 532 nm calibration unit is manufactured with polarizing film, providing a possible full 360 degree rotation with ±90 degree rotation for calibration. However, while the mo-

torized filter wheel used in the UV channel has 360 degrees of rotation, it has only six fixed positions. With one of those six used for measurements, that only leaves a potential five positions for calibration. As explained in chapter 3 only three of these five positions are needed. Unlike the 532 nm calibration this will only provide six measurement points and will hence be more susceptible to errors due to deterioration, such as shifts in alignment or filter damage, but easier to maintain as parts degrade over time.

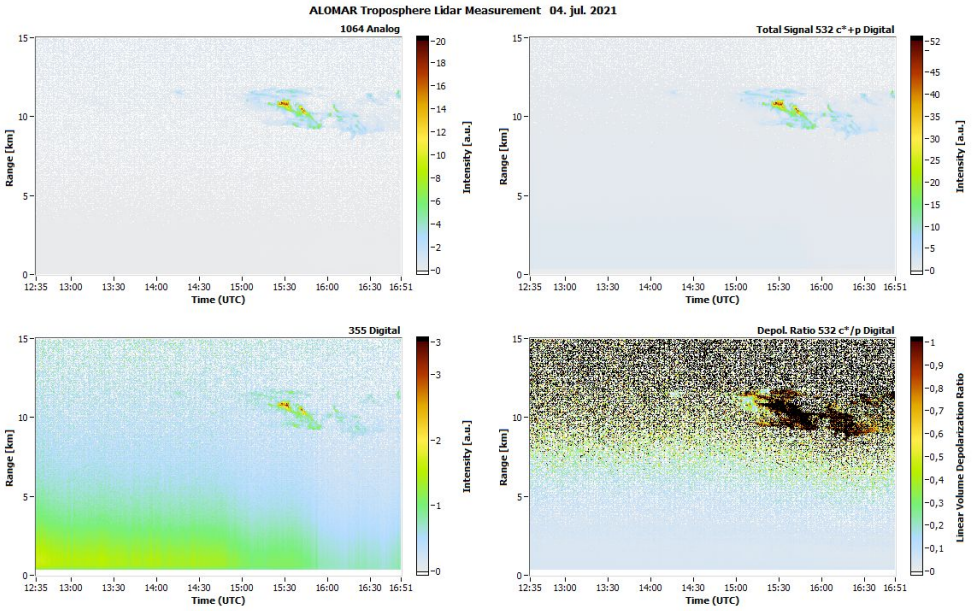

Figure 6.9: Labview plot from all channels on 4th of August 2021.

An overview of the different channel measurements on the 4th of August 2021 can be seen in figure 6.9. Of special note is the strong backscatter in the 355 nm channel at low altitude, but fading as the day progresses. While saturation of the system is represented by the white cutoff at very low altitudes, general low altitude lidar backscatter can be due to a number of reasons. The troposphere contains various aerosols such as dust, pollutants, and other particulate matter. At low altitudes, where the concentration of aerosols often is higher, the backscattered signal from the aerosols can become strong. Low-altitude clouds can significantly affect lidar measurements. Clouds are composed of water droplets or ice crystals that scatter and reflect light, including the laser pulses emitted by the lidar, this can also be seen from the cloud at 12-16 km height. When the lidar beam interacts with clouds at low altitudes, the return signals from the cloud particles can be intense. The ice-contents of the clouds could be investigated by comparing the results from the two depolarization channels to the papers by Kustova *et al.* [10, 11].

Interestingly the strong backscatter fades with a progressing day and this could be due to a number of reasons. For instance diurnal variation of aerosols. Aerosol

concentrations in the atmosphere can vary throughout the day due to factors such as human activities, local emissions, and meteorological conditions. If the aerosol loading responsible for the backscatter is higher in the morning or early hours and decreases as the day progresses, then lidar measurements may experience reduced backscatter at low altitudes later in the day. It could also be due to changing atmospheric conditions. The state of the atmosphere can change over the course of the day. For example, the mixing of air masses, atmospheric stability, and wind patterns can affect the distribution and characteristics of aerosols and clouds. If these conditions shift in a way that reduces the concentration or scattering properties of aerosols or clouds at low altitudes, it can lead to a decrease in backscatter as the day progresses. A shift in wind directing due to ground heating on a summer day carrying unpolluted, clean air from the north and north-western airmasses is an example of this and could be a likely culprit given the day of measurement was early August. If low-lying fog or clouds are present at low altitudes in the morning or early hours, they can contribute to backscatter in tropospheric lidar measurements. As the day progresses, solar heating, wind, or other atmospheric processes can lead to the dissipation or lifting of these fog or cloud layers, reducing the backscatter effects. Other environmental factors, such as temperature, humidity, and air pollution levels, can vary throughout the day. These factors can influence the formation, transport, and properties of aerosols and clouds. If conditions become more favorable for dispersion or dissipation of aerosols or clouds at low altitudes, it can result in a decrease in backscatter as the day progresses. An example of an environmental factor could be radiation fog or mist. During the night, the ground cools and can cause condensation on cloud-condensation nuclei. Typically such fogs or morning mists persists until the sun warms the ground and evaporates the fog.

Most of these reasons would imply a visible effect in all channels, but the strong signal is only visible in the 355 nm channel. Combining the thought of only visible in the 355 nm channel and fading as the day progresses provides a potential explanation. As lidar measurements at different wavelengths are sensitive to different particle sizes. The 355 nm channel, typically more sensitive to smaller aerosol particles, while the 532 nm and 1064 nm channels are more sensitive to larger particles. If the aerosols present in the atmosphere have a composition that results in stronger scattering at 355 nm, it can lead to a more intense return signal. Using the two depolarization channels as a wavelength pair the aerosols could be characterised by comparing results with the papers by Giannakaki *et al.* [12] and Müller *et al.* [13]. An investigation of a similar phenomena has been conducted by Gugerli, showcasing a diurnal fluctuation in the number and size of the aerosols, with more and marginally larger particles in the morning. Presumably some small water clusters formed overnight [50].

These explanations highlight the complexity of lidar measurements. The specific cause for the backscatter in the 355 nm channel, while the other channels re-

main unaffected, would require further investigation and analysis of the aerosol properties and atmospheric conditions on the day of measurement.

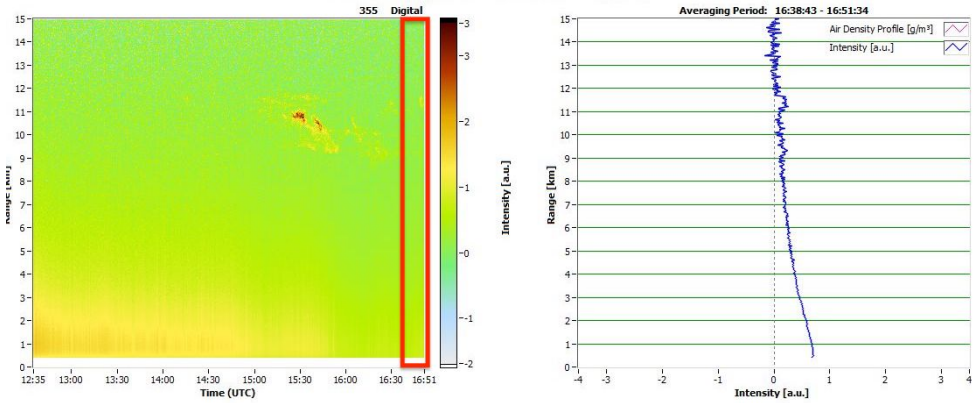

Figure 6.10: Labview plot from 355 nm channel on 4th of August 2021. Plot is averaged over the red outlined section.

As can be seen in figure 6.9 saturation in the 355 nm channel is reached earlier than the other channels, with even the digital channel seen in figure 6.10 reaching saturation around the same altitude as the 532 nm analog channel, figure 6.11. This either indicates the atmospheric conditions above ALOMAR favors scatter at shorter wavelengths, or could just be caused by Rayleigh scatter, which varies as λ^{-4}. Hence short wavelengths tend to scatter more than long, and could account for the 355 nm channel seeing more scattered sunlight.

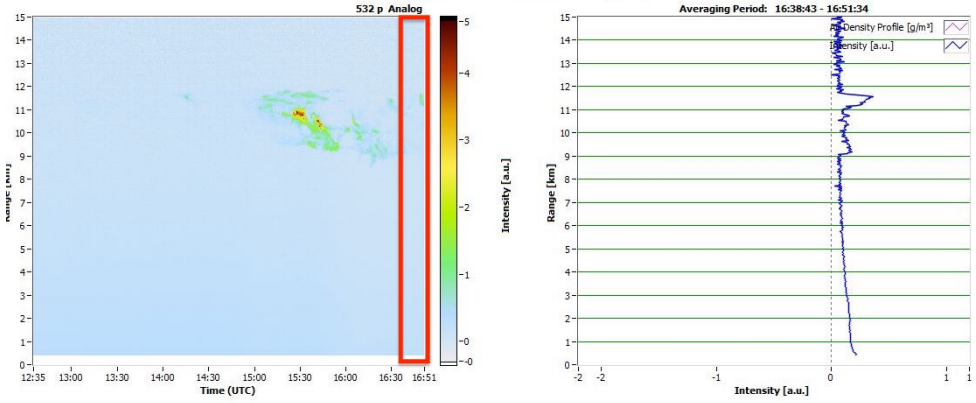

Figure 6.11: Labview plot from 532 nm channel on 4th of August 2021. Plot is averaged over the red outlined section.

As seen from both figure 6.10 and plot 6.11 part of the passing cloud is still within the averaged period and backscatter intensity peaks at 11-12 kms. Interestingly the intensity has a stronger peak in the 532 nm channel compared to the 355 nm channel. Given that water droplets scatter all wavelengths to a similar degree

this must be either due to the height of the cloud being advantageous for longer wavelength as less of the shorter wavelength reach the cloud, or due to particles or ice in the cloud scattering the visible 532 nm wavelength to a greater degree. The latter being the most likely explanation, as for a given wavelength, the scattering cross section as a function of $\frac{R}{\lambda}$ increases low values of $\frac{R}{\lambda}$, flattens off around $\frac{R}{\lambda}$=1, and then is reasonably flat for higher values of $\frac{R}{\lambda}$.

Chapter 7

Conclusion and future work

7.1 Conclusion

A design with benchmark tests for a 355 nm depolarization channel to characterize particles in the lowest part of the atmosphere, the troposphere, above ALOMAR has been presented. Theoretical background, data processing and analysis of existing measurements have also been displayed. The intended implementation of the depolarization channel encountered numerous problems and has not been installed. Solutions to all the aforementioned problems, have been proposed and the system is ready for installation as soon as the troposphere laser is operational.

7.2 Future work

- Implementation of 355 nm depolarization channel either in focal box as intended or in the detection box. Potentially also moving the 532 nm channel with the use of polarization maintaining fibers for easier access in the future.
- Test of polarization maintaining fibers influence on polarization
- Measurement comparison of 355 nm depolarization channel to EarthCARE satellite.
- Aerosol investigation and characterisation, comparison with the 532 nm channel, both for long and short term measurements.
- Investigate the Ångström exponent by use of the two depolarization channels.
- Calibration and systematic error calculation based on for instance the Müller-Stokes formalism.
- Comparison with the CIMEL sun photometers at ALOMAR.

Bibliography

[1] J. Salvesen, *Design of a uv 355 nm lidar depolarization channel to characterize particles in the atmosphere above alomar*, NTNU, 2022.

[2] P. Friedlingstein, M. O'Sullivan, M. W. Jones *et al.*, 'Global carbon budget 2022,' *Earth System Science Data*, vol. 14, no. 11, pp. 4811–4900, 2022.

[3] UNFCCC. 'The paris agreement.' `https://unfccc.int/process-and-meetings/the-paris-agreement/the-paris-agreement`. (2022). (accessed: 05.01.2022).

[4] G. Myhre, C. Lund Myhre, B. H. Samset and T. Storelvmo, 'Aerosols and their relation to global climate and climate sensitivity,' *Nature Education Knowledge*, vol. 4, p. 7, May 2013.

[5] IPCC, 'Synthesis report,' in *Climate Change 2001: Synthesis Report. A Contribution of Working Groups I, II, and III to the Third Assessment Report of the Intergovernmental Panel on Climate Change*, R. Watson, Ed., Cambridge, UK and New York, NY, USA: Cambridge University Press, 2001, pp. 1–398.

[6] J.-P. Putaud, R. Van Dingenen, A. Alastuey, H. Bauer, W. Birmili, J. Cyrys, H. Flentje, S. Fuzzi, R. Gehrig, H. Hansson and et al., 'A european aerosol phenomenology – 3: Physical and chemical characteristics of particulate matter from 60 rural, urban, and kerbside sites across europe,' *Atmospheric Environment*, vol. 44, no. 10, pp. 1308–1320, 2010.

[7] B. Holben, T. Eck, I. Slutsker, D. Tanré, J. Buis, A. Setzer, E. Vermote, J. Reagan, Y. Kaufman, T. Nakajima and et al., 'Aeronet—a federated instrument network and data archive for aerosol characterization,' *Remote Sensing of Environment*, vol. 66, no. 1, pp. 1–16, 1998.

[8] J. Hansen and A. Lacis, 'Sun and dust versus greenhouse gases - an assessment of their relative roles in global climate change,' *Nature*, vol. 346, Sep. 1990.

[9] M. Frioud, M. Gausa, G. Baumgarten, J. E. Kristjansson and I. Føre, 'New tropospheric lidar system in operation at alomar (69°n, 16°e),' *Proceedings of 23rd International Laser Radar Conference*, pp. 179–182, 2006.

[10] N. Kustova, A. Konoshonkin, V. Shishko, D. Timofeev, I. Tkachev, Z. Wang and A. Borovoi, 'Depolarization ratio for randomly oriented ice crystals of cirrus clouds,' *Atmosphere*, vol. 13, no. 10, p. 1551, 2022.

[11] N. Kustova, A. Konoshonkin, V. Shishko, D. Timofeev, Z. Wang and A. Borovoi, 'Coherent backscattering by large ice crystals of irregular shapes in cirrus clouds,' *Atmosphere*, vol. 13, no. 8, p. 1279, 2022.

[12] E. Giannakaki, P. Zyl, D. Müller, D. Balis and M. Komppula, 'Optical and microphysical characterization of aerosol layers over south africa by means of multi-wavelength depolarization and raman lidar measurements,' *Atmospheric Chemistry and Physics*, vol. 16, pp. 8109–8123, 2016.

[13] D. Müller, C. Böckmann, A. Kolgotin, L. Schneidenbach, E. Chemyakin, J. Rosemann, P. Znak and A. Romanov, 'Microphysical particle properties derived from inversion algorithms developed in the framework of earlinet,' *Atmospheric Measurement Techniques Discussions*, vol. 8, pp. 12 823–12 885, 2015.

[14] A. Miffre, D. Cholleton and P. Rairoux, 'On the use of light polarization to investigate the size, shape, and refractive index dependence of backscattering ångström exponents,' *Optics Letters*, vol. 45, no. 5, pp. 1084–1087, 2020.

[15] D. Hua, M. Uchida and T. Kobayashi, 'Ultraviolet high-spectral-resolution rayleigh–mie lidar with a dual-pass fabry–perot etalon for measuring atmospheric temperature profiles of the troposphere,' *Optics Letters*, vol. 29, no. 10, pp. 1063–1065, 2004.

[16] A. P. Cracknell and L. Hayes, *Introduction to remote sensing* (2). CRC Press, 2007, ISBN: 978-0-8493-9255-9.

[17] F. L. Pedrotti, L. M. Pedrotti and L. S. Pedrotti, *Introduction to Optics* (3). Cambridge University Press, 2018, ISBN: 9781108597548.

[18] C. Weitkamp, Ed., *Lidar: Range-resolved optical remote sensing of the atmosphere* (102). Springer Science, 2005, ISBN: 0-387-40075-3.

[19] A. T. Young, 'Rayleigh scattering,' *Physics Today*, vol. 35, no. 1, pp. 42–48, 1982.

[20] C. She, 'Spectral structure of laser light scattering revisited: Bandwidths of nonresonant scattering lidars,' *Applied Optics*, vol. 40, no. 27, pp. 4875–4884, 2001.

[21] J. Li, B. E. Carlson, Y. L. Yung, D. Lv, J. Hansen, J. E. Penner, H. Liao, R. Ramaswamy, R. A. Kahn, P. Zhang, O. Dubovik, A. Ding, A. A. Lacis, L. Zhang and Y. Dong, 'Scattering and absorbing aerosols in the climate system,' *Nature Reviews Earth & Environment*, vol. 3, no. 6, pp. 363–379, 2022.

[22] U. von Zahn, G. von Cossart, K. H. Fiedler J. Fricke, G. Nelke, G. Baumgarten, D. Rees, A. Hauchecorne and K. Adolfsen, 'The alomar rayleigh/mie/raman lidar: Objectives, configuration, and performance,' *Annales Geophysicae*, vol. 18, no. 7, pp. 815–833, 2000.

[23] J. D. Klett, 'Stable analytical inversion solution for processing lidar returns,' *Applied Optics*, vol. 20, no. 2, pp. 211–220, 1981.

[24] P. Piironen, 'A high spectral resolution lidar based on an iodine absorption filter,' Ph.D. Thesis, University of Joensuu, Department of Physics , Finland, 1994.

[25] A. Ångström, 'Techniques of determining the turbidity of the atmosphere,' *Tellus*, vol. 13, pp. 214–223, 1961.

[26] C. Toledano, V. Cachorro, A. Berjón, M. Sorribas, R. Vergaz, Á. D. Frutos, M. Antón and M. Gausa, 'Aerosol optical depth at alomar observatory (andøya, norway) in summer 2002 and 2003,' *Tellus B: Chemical and Physical Meteorology*, vol. 58, no. 3, pp. 218–228, 2006.

[27] E. Rodriguez, M. Frioud, M. Gausa, K. Stebel, S. Mogo, N. Prats, B. Torres, C. Toledano, Á. Bastidas, A. Berjón, V. Cachorro and Á. M. Frutos, 'Optical properties of tropospheric aerosols derived from lidar and sun photometer measurements at alomar (69n) in 2005 and 2006,' *ÓPTICA PURA Y APLICADA*, vol. 41, no. 2, pp. 183–190, 2008.

[28] F. Kasten and A. T. Young, 'Revised optical air mass tables and approximation formula,' *Applied Optics*, vol. 28, no. 22, pp. 4735–4738, 1989.

[29] P. Fimpel, 'Depolarized lidar measurements at alomar: Improvments of the data quality due to the laser warm up phase and atmospheric changes,' Bachelor's Thesis, University of Constance, 2012.

[30] P. P. Urone and R. Hinrichs, *College Physics*. OpenStax, 2012, ISBN: 978-1-947172-01-2.

[31] M. Gadsden and W. Schröder, 'Noctilucent clouds,' in *Noctilucent Clouds*. Springer Berlin Heidelberg, 1989, pp. 1–12, ISBN: 978-3-642-48626-5.

[32] V. Freudenthaler, 'About the effects of polarising optics on lidar signals and the 90 calibration,' *Atmospheric Measurement Techniques*, vol. 9, no. 9, pp. 4181–4255, 2016.

[33] Y. Zhao, A. Boselli, L. Nasti, G. Pisani, N. Spinelli and X. Wang, 'Polarization lidar calibration techniques and sensitivity analysis,' *International Journal of Remote Sensing Applications*, vol. 3, no. 4, pp. 251–257, 2013.

[34] Z. Sun, Q. Cheng, Y. Hui, M. Jiang, H. Lei and Q. Li, 'Enhancing extinction ratio of polarization and pulse stability simultaneously from passively q-switched [100]-nd:yag/[110]-cr4+:yag laser,' *Optics Communications*, vol. 335, pp. 245–249, 2015.

[35] Edmund-Optics, *What are beamsplitters?: Edmund optics*. [Online]. Available: `https://www.edmundoptics.com/knowledge-center/application-notes/optics/what-are-beamsplitters/`, (accessed: 01.12.2022).

[36] Thorlabs, *High-power, laser line, polarizing beamsplitter cubes*. [Online]. Available: `https://www.thorlabs.de/newgrouppage9.cfm?objectgroup_id=6055$%5C&$amp;pn=PBS25-355-HP`, (accessed: 01.12.2022).

[37] Edmund-Optics, *355nm, 25mm diameter, thin film laser line polarizer*. [Online]. Available: https://www.edmundoptics.com/p/355nm-25mm-diameter-thin-film-laser-line-polarizer/29111/, (accessed: 01.12.2022).

[38] Spectrogon, *Filter cwl shift as function of aoi and temperature*. [Online]. Available: https://www.spectrogon.com/products/optical-filters/filter-cwl/#of_target, (accessed: 01.12.2022).

[39] G. R. Rowles, *Introduction to Modern Optics* (2). Courier Corporation, 1989, ISBN: 0-486-65957-7.

[40] H. B. Wach, E. R. Dowski and W. T. Cathey, 'Control of chromatic focal shift through wave-front coding,' *Applied Optics*, vol. 37, no. 23, pp. 5359–5367, 1998.

[41] Thorlabs, *Thorlabs - pm-s350-hp 350 - 460 nm pm fiber w/ pure silica core, 0.12 na, 2.3 μm mfd*. [Online]. Available: https://www.thorlabs.com/thorproduct.cfm?partnumber=PM-S350-HP, (accessed: 01.12.2022).

[42] F. A. Jenkins and H. E. White, *Fundamentals of Optics* (2). McGraw-Hill Book Company, 1950.

[43] Newport, *Light detection and ranging (lidar)*. [Online]. Available: https://www.newport.com/n/lidar, (accessed: 01.12.2022).

[44] V. A. Kovalev and W. E. Eichinger, *Elastic Lidar: Theory, Practice, and Analysis Methods*. John Wiley & Sons, Inc., 2004, ISBN: 0-471-20171-5.

[45] B. Mielke, *Analog + photon counting*, https://licel.com/manuals/analogpc.pdf, (accessed: 21.11.2022).

[46] W. Wolfgang, A. Ullrich, V. Ducic, T. Melzer and N. Studnicka, 'Gaussian decomposition and calibration of a novel small-footprint full-waveform digitising airborne laser scanner,' *ISPRS Journal of Photogrammetry and Remote Sensing*, vol. 60, no. 2, pp. 100–112, 2006.

[47] J. L. Guerrero-Rascado, R. Facundes da Costa, A. E. Bedoya, R. Guardani, L. Alados-Arboledas, Á. E. Bastidas and E. Landulfo, 'Multispectral elastic scanning lidar for industrial flare research: Characterizing the electronic subsystem and application,' *Optics Express*, vol. 22, no. 25, pp. 31 063–31 077, 2014.

[48] Bentham, *Cl-hg wavelength calibration standard (250-600nm)*. [Online]. Available: https://www.bentham.co.uk/products/components/cl-hg-wavelength-calibration-standard-250-600nm-24/#specifications, (accessed: 23.05.2022).

[49] CMS - ING. DR. SCHREDER GMBH, *J1004-sma*, http://www.schreder-cms.com/en_pdf/J1004-SMA.pdf, (accessed: 28.02.2022).

[50] R. Gugerli, *Controlling factors for aerosol optical depth in trondheim*, NTNU, 2012.

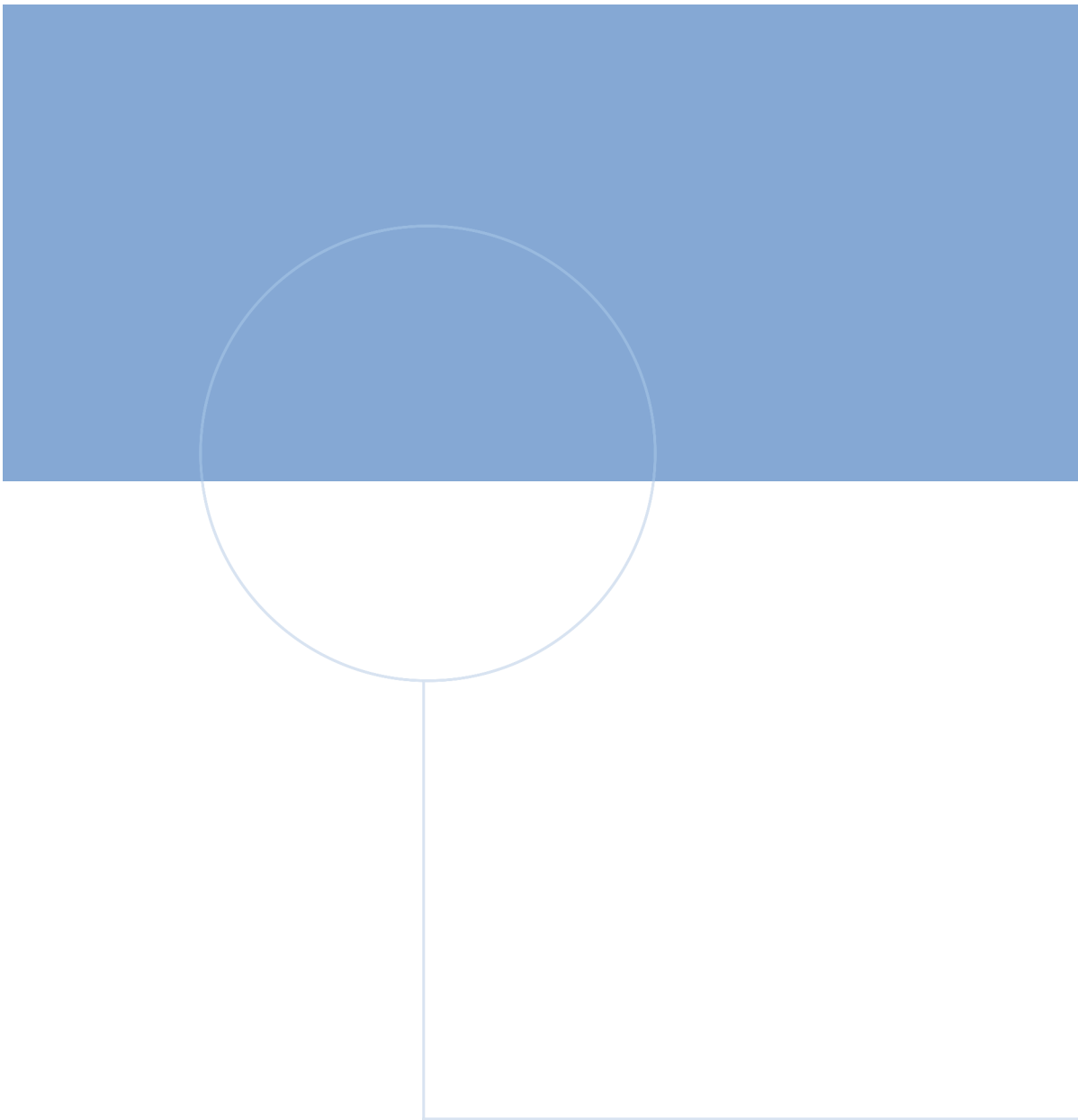

NTNU

Norwegian University of
Science and Technology